Charles University in Prague
Faculty of Mathematics and Physics

DIPLOMA THESIS

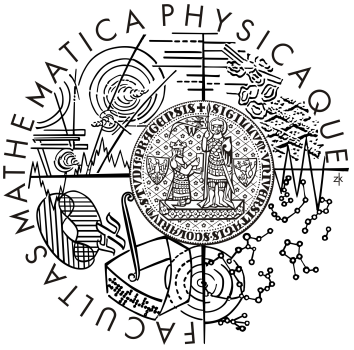

Miroslav Vácha

Detection systems for measurements of high-temperature plasma radiation on the COMPASS tokamak by fast bolometers and soft X-ray detectors

Institute of Particle and Nuclear Physics

Supervisor: Mgr. Vladimír Weinzettl, Ph.D.
(Institute of Plasma Physics AS CR, v.v.i.)

Study program: Nuclear and subnuclear physics

2009

I am very grateful to my advisor Mgr. Vladimír Weinzettl, Ph.D. for his patient and careful guidance.

I declare that I have worked out this thesis by myself using only the literature cited here. I agree with lending of this thesis from the library of Faculty of Mathematics and Physics.

Prague, April 16, 2009 Miroslav Vácha

Contents

Název práce: Detekční systémy pro měření vyzařování vysokoteplotního plazmatu tokamaku COMPASS na bázi rychlých bolometrů a měkkých rentgenových detektorů
Autor: Miroslav Vácha
Katedra: Ústav částicové a jaderné fyziky
Vedoucí práce: Mgr. Vladimír Weinzettl, Ph.D., Ústav fyziky plazmatu AV ČR v.v.i.
e-mail vedoucího: vwei@ipp.cas.cz

Abstrakt: Mnohokanálová spektroskopická diagnostika pro tokamak COMPASS na bázi AXUV bolometrů, měkkých rentgenových detektorů a detektorů viditelného světla pokrývá široké spektrum vyzařování tokamakového plazmatu a umožní rychlou tomografii v mikrosekundových časových škálách. Práce shrnuje vývoj bolometrické a měkké rentgenové diagnostiky. Nejprve je diskutován výběr detektorů a jejich testy. Dále je shrnut návrh kombinované vložky do diagnostického portu, která umožňuje umístit oba systémy do velmi malého prostoru a zároveň jim poskytuje chlazení a stínění v průběhu procedur čištění komory. Rovněž je dokumentován vývoj nových zesilovačů signálu a jejich zapojení do systému sběru dat. V závěrečných kapitolách jsou prezentovány základní metody analýzy dat z těchto diagnostických systémů.
Klíčová slova: tokamak, vyzařování plazmatu, fotodioda, tomografie

Title: Detection systems for measurements of high-temperature plasma radiation on the COMPASS tokamak by fast bolometers and soft X-ray detectors
Author: Miroslav Vácha
Department: Institute of Particle and Nuclear Physics
Supervisor: Mgr. Vladimír Weinzettl, Ph.D., Institute of Plasma Physics AS CR, v.v.i.
Supervisor's e-mail address: vwei@ipp.cas.cz

Abstract: Multi-channel spectroscopic diagnostics on the COMPASS tokamak comprising AXUV-based bolometers, soft X-ray (SXR) and visible light detectors will cover a wide spectral range of the core and edge plasma emission, aiming to realize a fast tomography at microsecond time scales. This thesis reports on a development of the bolometric and SXR diagnostics. First, procedures of the detector selection and their tests are described. There the design and tests of the special complex port plug, combining both detection systems, taken into account a strongly limited available space, a heat protection and a shielding during a cleaning glow discharge, is also summarized. Development of new electronic amplifiers and their connection with the data acquisition system is documented. In the last chapters, basic methods for analysis of data collected using these diagnostic systems are introduced.
Keywords: tokamak, plasma radiation, photodiode, tomography

Chapter 1

Introduction

The main aim of the fusion research is a development of the thermonuclear reactor - a fusion power plant. To ignite a thermonuclear synthesis in such a device it is necessary to put together fusing nuclei close enough to overcome strong repulsive electrostatic forces originating in an interaction between positively charged atomic nuclei. To pass these forces a thermal energy of chaotic movement of particles at extremely high temperatures can be used. Fusion reactions release by orders more energy than it is necessary for ignition.

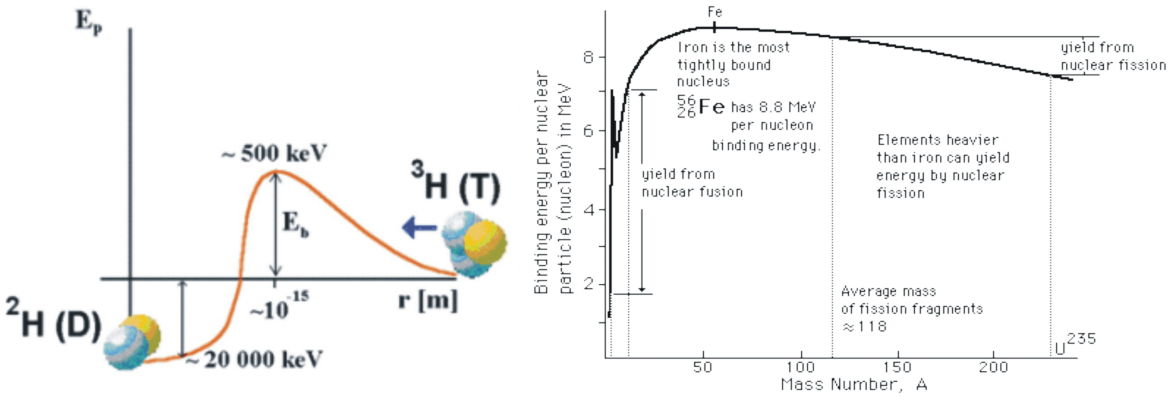

Figure 1.1: *Dependence of hydrogen nuclei repulsion on distance between them (left), dependence of binding energy per nucleon on atomic number (right)*

1.1 Tokamak concept

A tokamak device is the most hopeful present concept realizing thermonuclear fusion of light atomic nuclei (Z $\sim$ 1) at high temperatures (T $>$ 10^7K) and high densities of charged particles (10^{18} m^{-3} $<$ n $<$ 10^{20} m^{-3}), i.e. conditions suitable for carrying out fusion reactions. At that time, matter becomes highly ionized plasma. Its electrically charged particles are confined inside a vacuum vessel of the tokamak by a strong magnetic field (B $>$ 1T).

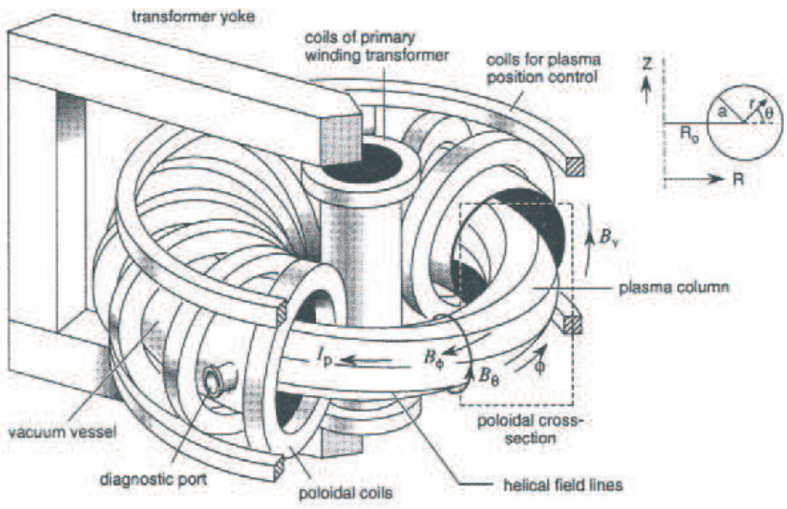

Figure 1.2: *Principal scheme of tokamak*

A principle of the tokamak device is relatively close to a collider, where charged particles are confined by a strong magnetic field in a vacuum vessel. In a collider, the number of particles is very low in order to prohibit interactions between them. Consequently, particle confinement is close to ideal and a single particle approximation describes a reality very well. On the other hand, in tokamaks and other fusion devices, a collective behaviour of charged particles plays a dominant role as a result of a high concentration (density) of charged particles. This state of matter is called plasma (for more details see [1],[2]).

1.2 Tokamak COMPASS-D

The COMPASS-D (COMPact ASSembly) device was designed as a flexible tokamak in the 1980s in Culham mainly to explore MHD physics in circular and D - shaped plasmas. Its operation began at the Culham Laboratory of the Association EURATOM/UKAEA in 1989. In 2001 it was decided to mothball COMPASS-D in Culham and in 2001 it was offered to IPP Prague by UKAEA.

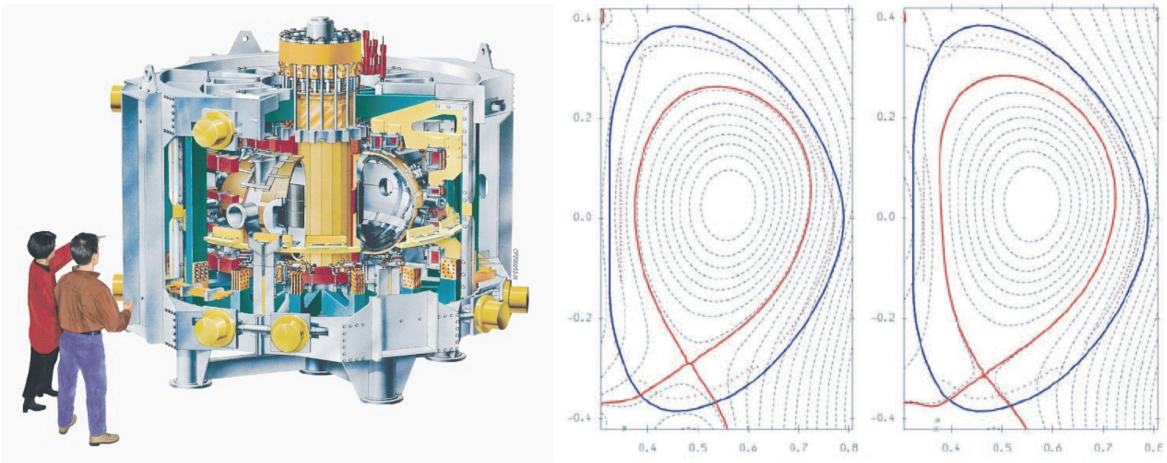

Figure 1.3: *Scheme of COMPASS-D tokamak (left), examples of ITERlike shapes of plasma in COMPASS-D (right)*

COMPASS-D tokamak is equipped with a unique four quadrant set of copper saddle coils to create resonant helical fields. A hydraulic vertical preload has to be used for toroidal magnetic field above 1.2 T. The COMPASS-D tokamak has an ITER-like plasma shape and, after installation of an ion heating system, it will be able to access plasma parameters relevant in many aspects to ITER. It will be an ideal device for detailed studies of edge plasma physics in the H-mode regime (e.g., pedestal, ELMs, turbulence, etc.)

A working gas in the COMPASS tokamak is hydrogen (now light isotope ^{1}H, in future deuterium). A purity of used hydrogen is critical, because only few percents of impurities can evoke a disruption of the discharge or even can cool down a plasma by a strong radiation. A working pressure of hydrogen before the discharge is about 10^{-2}Pa. During the discharge a pulse gas puffing through a fast piezoelectric valve is possible. Cleanness of the tokamak chamber is provided by rotary and turbo-molecular pumps up to pressure 10^{-8}Pa. Next methods, how to remove a residual gas from the vacuum

chamber are a glow discharge and a baking, which are used mainly after an opening of the chamber. At temperatures 200-300°C an outgassing is done. For more informations see [3].

R	0.56 m
a	0.18 ÷ 0.23m
I_p(max)	200kA
B_T(max)	1.2 ÷ 2.1T
Discharge time	1s
Proportion to ITER plasma	1:10

Table 1.1: *Main parameters of the COMPASS tokamak*

1.3 Motivation for radiation measurements

Physical knowledge, in plasma confinement and particle/energy transport relevant to design of a commercial tokamak-based fusion power plant, still contains a high degree of uncertainty in description of extremely high escape of particles/energy from a high-temperature plasma region. A precise theory of the classical collisional transport losses has been developed. Since this does not completely explain the transport processes across magnetic surfaces, additional processes driven by plasma turbulent structures were required to be taken into account. The theoretical picture of turbulence-induced transport is that the free energy released by instability drives a steady level of fluctuations in the associated perturbed quantities. In this turbulent state, fluctuations result in a radial transport of particles and energy. To understand more properly the effect of anomalous diffusion found at the edge tokamak plasma, an intense activity based on focused experiments, theory development and modeling effort has been carried out at tokamaks with the aim of advancing transport understanding.

A physical substance of the particle/energy transport in the tokamak plasma can be studied in details very advantageously using spectroscopic tools with sufficient temporal and spatial resolution. Such approach can be represented by tomographic techniques applied on fast bolometric, soft X-ray or visible light measurements. In the last years, a fast progress in the development of fine spectroscopic tools with high temporal and spatial resolution could be registered. Together with parameters improvement of used detection systems, a great advance in computer simulations permits to make comparative studies between theoretical models and experimental results leading to the optimization of tokamak discharge regimes.

In case of COMPASS tokamak the main objective is to design and construct the multi-range high resolution tomographic systems for fast events detection in tokamak plasma and subsequently use this apparatus for a measurement and characterization of these plasma structures in the COMPASS tokamak. Spatially resolved measurements give indirect information on a plasma position and its profile. Processes connected with a radial particle/energy transport (e.g. instabilities, creation of transport barriers, radiation islands) often express themselves as fast changes in a radiation and can be studied using detection systems with a sufficiently high temporal resolution.

Moreover, the integral bolometric measurements of total radiated power during a tokamak discharge allow estimating both the fraction of input power lost via plasma radiation, and the effective plasma charge. The integral soft X-ray diagnostic is suitable for computation of plasma temperature, impurity studies, and monitoring of core activity (sawteeth ...)[4].

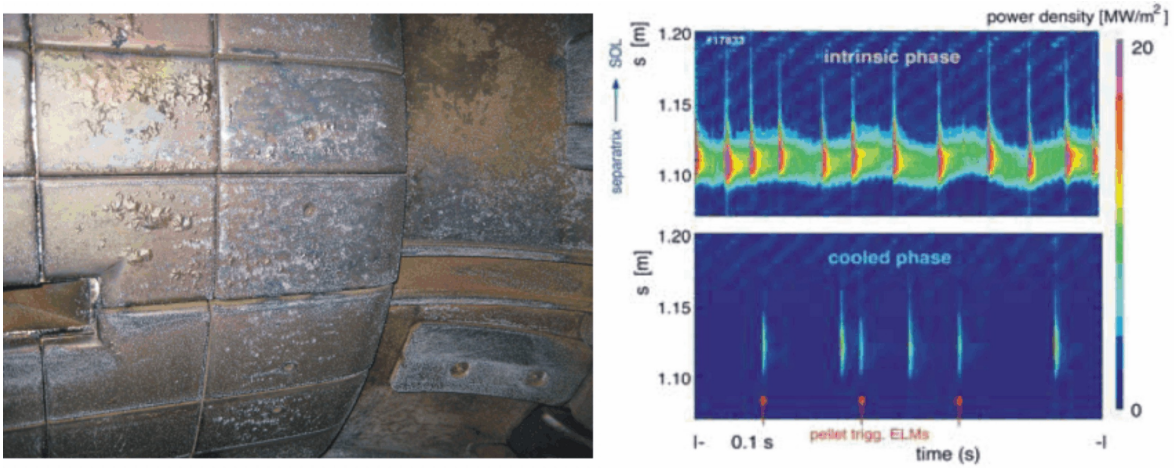

Figure 1.4: *Damage of the first wall on Compass tokamak (left), comparison of power losses in the divertor region with and without radiation cooling on Asdex tokamak (right) [5]*

On the other hand, plasma radiation can be also used for the so called radiation cooling, which minimizes an erosion of the divertor plates. Using this method, mainly noble gasses (e.g. argon) are injected in the divertor region in order to absorb the energy of "hot" particles, which is subsequently re-radiated into the wider solid angle (see [5],[6]).

Chapter 2

Plasma radiation

Spectrum of electromagnetic radiation emitted by tokamak plasma is composed of both discrete (line) and continuous contributions over a wide range of energies. The biggest part falls into ultraviolet (UV) and soft X-ray (SXR) regions, which means energies about 10-10^4eV. With a growth of electron temperature a portion of X-ray in the total plasma radiation is increasing. This chapter provides a brief review of radiation processes occurring in typical tokamak plasma.

2.1 Theory

Radiation processes in tokamak plasmas are mainly represented by electron transitions and can be classified by a state of the electron before and after the interaction. Line radiation is caused by bound-bound transitions of electrons in atoms and not-fully-ionized ions, in which electrons lose their energy going closer to the ground state. Radiation can also be emitted when a free electron is accelerated in electric field. This process leads to a free-free transition (also called bremsstrahlung, continuous radiation) and the electron stays free. When an accelerated electron meets a bound electron, a free-bound transition (recombination radiation) is realized causing continuous and often also line radiation.

Line radiation

The emission of line radiation proceeds due to the transition of electrons between bound states in atom or ion. It is obvious that it has discrete character. The dominant level population mechanisms are electron-impact excitation and de-excitation.

In tokamak plasma some partially stripped ions can be always found. At the edge of the plasma, the temperature is only few eV and therefore even atoms with low Z as hydrogen may not be fully ionized here, because both a high influx of neutrals from nearby walls is present and recombination processes occur. Impurities like iron (Z=26) or tungsten (Z=74) have higher ionization potentials and therefore they are not fully stripped even in the "hot" centre of the plasma (temperatures about some keV).

Considering a number of possible electron transitions and all species of impurities being involved, the total line radiation covers up a wide energy range and very different intensities. The power density for line radiation is given by summation over all present elements and states:

$$P_{bb} = \sum_{element} \sum_{state} n_e n_z \sum_{i,j} \hbar\omega_{ij} \frac{A_{ij}}{\sum_{k<j} A_{ik}} \langle \sigma_{ij}.\nu_e \rangle \quad \left[W m^{-3} \right] \tag{2.1}$$

where A_{ij} are the transition probabilities, n_e and n_z are the electron and ion densities, σ_{ij} is the cross section for electron excitation and the average $\langle . \rangle$ is done over the electrons distribution. For more details about the line radiation in general, see [7]; for more information about the plasma line radiation, see [8].

Bremsstrahlung

Bremsstrahlung is emitted by a charged particle which is accelerated in electric field of another charged particle. As mentioned above in case of tokamak plasma, the accelerated particle is an electron deflected by an ion. Due to the free electron have a continuum of energy states, the free-free transition give rise to a continuum (in energy) of radiation.

The bremstrahlung power density per unit photon energy interval can be written as:

$$\frac{dP_{ff}}{dE} = 1.54 \times 10^{-38} n_e Z^2 \overline{g_{ff}} \frac{e^{-E/T_e}}{\sqrt{T_e}} \quad \left[W m^{-3} eV^{-1} \right] \tag{2.2}$$

where E is the photon energy, Z is the ion charge, n_e electron density, T_e electron temperature and $\overline{g_{ff}} = \overline{g_{ff}}(E, T_e, Z)$ is the free-free transition Gaunt factor averaged over a Maxwellian electron velocity distribution. Factual values of $\overline{g_{ff}}$ are tabulated in [9].

To obtain the total bremsstrahlung emission, this expression must be summed over all ions present in the plasma. The total bremsstrahlung power density per unit energy interval is

$$\frac{dP_{ff}^{total}}{dE} = 1.54 \times 10^{-38} n_e Z_{eff} \overline{g_{ff}} \frac{e^{-E/T_e}}{\sqrt{T_e}} \quad \left[W m^{-3} eV^{-1} \right] \tag{2.3}$$

where the effective ion charge is defined as:

$$Z_{eff} = \sum Z \frac{n_z Z^2}{n_e} \tag{2.4}$$

with the summation extending over all ionization states of all species. A measure of the impurity content of the plasma is Z_{eff}, with $Z_{eff} = 1$ for a pure hydrogen plasma. The factor Z_{eff} in equation 2.3 express the enhancement of the bremsstrahlung emission due to impurities in hydrogen plasma. For more details see [10], [11] or [12].

Recombination radiation

When a free electron is captured to the bound state of an ion the recombination radiation is emitted. This process is also called free-bound transition. There are two types of recombination transitions - radiative and dielectronic recombination.

In case of radiative recombination free electron is captured to the bound state of ion and subsequently radiated energy is in the form of electromagnetic quantum. The energy is determined by incoming electron energy and the ionization potential of appropriate ion, what indicates that the energy spectrum is continuous.

The expression for the power density per unit photon energy due to recombination radiation is more complex because summation over electron transitions from the continuum to all bound states of the ions is required:

$$\frac{dP_{fb}}{dE} = 1.54 \times 10^{-38} n_e Z^2 \overline{g_{fb}} \frac{e^{-E/T_e}}{\sqrt{T_e}} \beta(Z, T_e) \quad \left[W m^{-3} e V^{-1} \right] \tag{2.5}$$

where $\overline{g_{fb}} = \overline{g_{fb}}(E, T_e)$ is the Maxwellian averaged free-bound Gaunt factor [9] and the factor $\beta(Z, T_e)$ is a complex expression incorporating the summation over possible transitions. More can be found in [11] or [12].

On the other hand, the spectrum of dielectronic recombination is discrete. In this process, the non-radiative capture of electron to the high excited bound state of ion occurs and the energy is radiated subsequently. Autoionisation or the stabilisation process may proceed. Stabilisation means cascade transition between bound states. Detailed insight to the dielectronic recombination theory can be found in [13].

2.2 The full radiation spectrum

The real radiation spectrum is sum of here presented processes. In pure hydrogen plasma the bremsstrahlung component strongly dominates. But even a small amount of nuclei

with high Z (e.g. Fe, W) causes that the portion of recombination radition strongly increases. In dirty plasma also peaks originating from line radiation are visible and they dominate the emission in regions, where they occur.

In fig.2.1 the calculated SXR radiation spectrum is shown. The comparison of spectra of pure hydrogen plasma and 1% Fe impurity is ploted. The contributions of each radiation processes are accentuated.

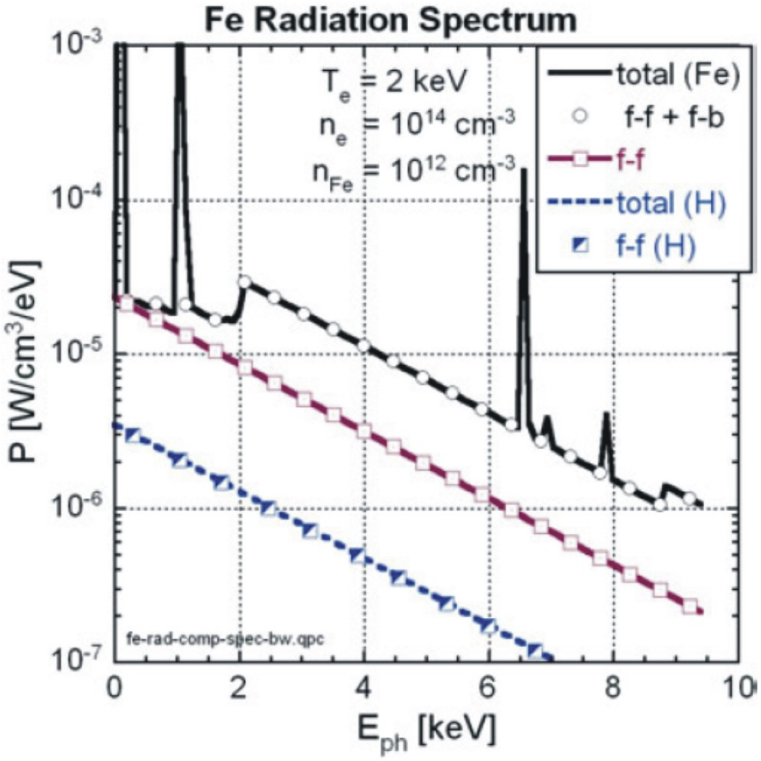

Figure 2.1: *Calculated SXR spectrum of iron showing the contributions of line, bremsstrahlung, and radiative recombination radiation. The hydrogen continuum is shown for comparison [14].*

Chapter 3

Detectors

The knowledge of the total radiated power is essential for the control and understanding of the power balance in tokamaks. An assembly of multichannel bolometers and SXR detectors viewing inside the vessel through a pinhole camera and whose chords are covering the whole cross section of the plasma permits the reconstruction of emissivity profile with sufficient spatial and temporal resolution. Selection of detectors and properties of the chosen ones will be depictured in this chapter.

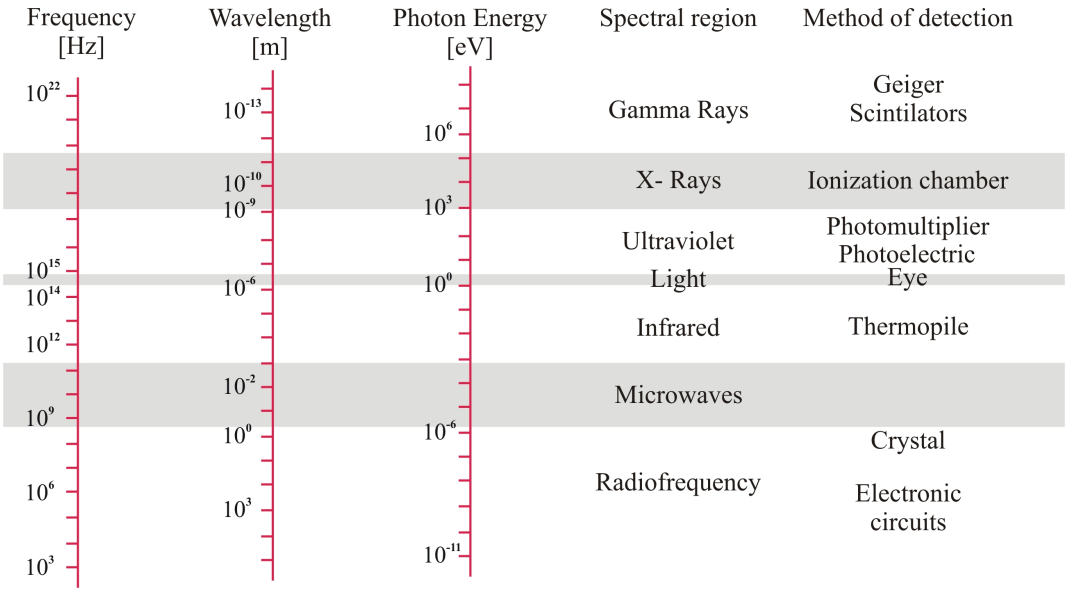

Figure 3.1: *The electromagnetic spectrum and methods of detection*

Detectors suitable for use on tokamaks have to satisfy several requirements. During the baking of the vacuum vessel detectors in diagnostic port should survive high temperatures. They must be capable of operation in ultrahigh vacuum ($\sim 10^{-8}$ Pa) and in high magnetic fields. Furthermore, they have to be resistant against radiation damages, especially neutrons escaping the plasma. Next, they need an effective rejection of background signals whose origin may be found in temperature change of their support, volume absorption of nuclear radiation, common-mode voltage or electromagnetic pickup. During experimental campaigns on tokamak the access to the installed detectors is limited or completely impossible and therefore a high reliability is a prerequisite. For tomographic investigation of plasmas a larger number of detectors are necessary and their calibration must be easily reproducible. Of course, the calibration data cannot show a temporal drift. Therefore calibration in situ is desirable.

3.1 Bolometers

Bolometric measurements provide information about total radiated power [15]. In fact, there are two types of bolometers operating on different physical principles: thermal bolometer and semiconductor bolometer (AXUV detector), which characteristics are descibed in next sections.

3.1.1 Thermal bolometers

Operational principle of this sort of bolometers is based on the absorption of the radiation leading to a temperature rise of the absorber and measuring this change. All these detectors have in fact a relatively rough temporal resolution ($\sim$10ms), despite it they are widely used in plasma diagnostic.

So called metal foil bolometers consist of a support sandwiched by a gold absorber foil and temperature measuring element on the other side. Support has to be a robust and reliable material that shows good mechanical strength and electrical insulation which are not degraded even after having received high radiation doses. The thickness of the gold foil is a compromise between the ability to sufficiently stop soft X-ray radiation and achievements of high sensitivity and short rise times. The ideal thickness is about some μm. A 4μm thick gold foil absorbs soft X-ray up to an energy about 5 keV. The second side element is typically a gold resistor measuring the temperature.

Gold has almost linear response to radiation down to 5eV, where the reflectivity increases dramatically. Neutrals are taken into account in the range of 20 eV up to 1 keV. Charged particles, neutrons, radiation and hard X-ray don't contribute to the

bolometer signal. Blackened absorber surfaces extend the measurable radiation down to infrared. A rougher surface provides better absorption for neutrals.

Calibration of metal foil detector can be simply performed by self-heating. Using pulse voltage source a known ohmic power is dissipated in the gold resistor, what can be done remotely when mounted in diagnostic port. Metal foil bolometers may be baked up to 300°C.

The biggest disadvantage of these detectors is temporal resolution of typically 10ms. On the other hand metal foil bolometers have the detection limit approximately 5 times higher (about $100\mu W/cm^2$) than semiconductor bolometers.

There is one more type of thermal bolometer - pyroelectric bolometer, which is also often used. In contrast to metal foil bolometers these detectors measure the temperature change of the absorber by pyroelectric element. Some materials (e.g. $LiTaO_3$) exhibit temperature-dependent spontaneous polarization, which leads to changes on the surface of the material and can be measured as a current when the element is integrated in the electric circuit. The properties are similar as in case of metal foil detectors.

3.1.2 Semiconductor detectors - AXUV photodiodes

Silicon photodiodes are operating on principle of inner photo effect. The energy from incident photon is absorbed by photodiode atom and subsequently an electron is emitted (the atom is ionized). This free electron is colliding with other electrons and produces next electron-hole pairs. Impact of the photon thus evokes creation of electric current. Its size depends on energy of incoming photon.

This new generation of detectors uses silicon p-n junction photodiodes. Figure 3.2 shows the n-type layer deposited on the p+type wafers. On the upper side the active region is formed by a SiO_2 (glass) passivating window of 3 to 7 nm of thickness. The field oxide surrounding the active surface is used to create the internal electric field. AXUV stands for Absolute eXtreme UltraViolet-detector.

The first ionization energy of silicon is 3.65 eV and theoretically an incident photon having this energy (or greater) permits the creation of an electron-hole pair in the depletion zone. Due to the internal electric field, electron and hole run in opposite direction, generating a current in an external circuit. In practice the probability of electron-hole carriers created per incident photon of energy E is characterized by the quantum efficiency χ (see figure 3.3 with experimental data delivered by the manufacturer). Already an energy of 1.12 eV may create an electron-hole pair (but with poor probability). For photon energies greater than 3.7 eV more than one carrier pair is generated, increasing

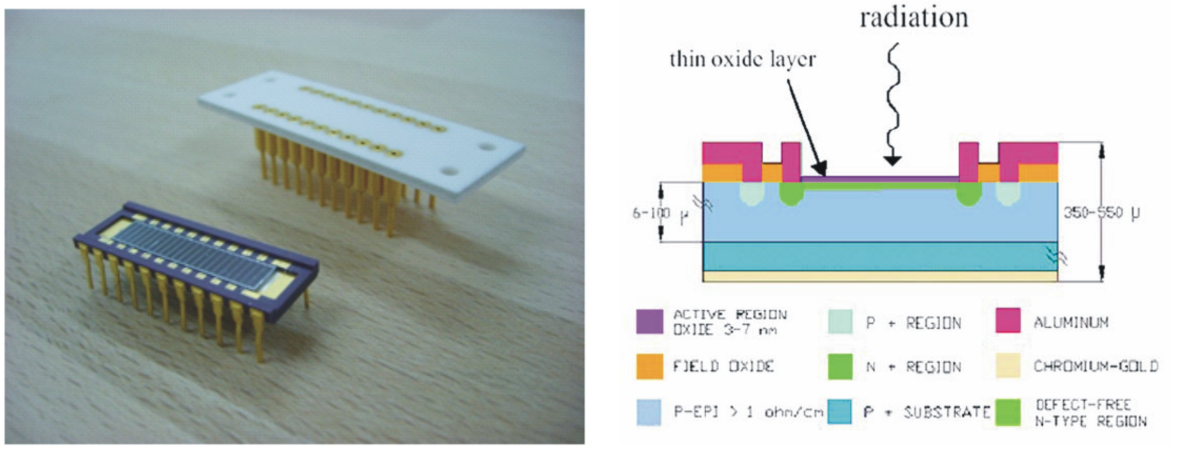

Figure 3.2: *AXUV20ELM detector with ceramic socket (left); Layering of the AXUV-detector (right) [16]*

almost linearly with energy, satisfying the theoretical relation:

$$\chi = \frac{E[eV]}{3.65[eV]} \tag{3.1}$$

The loss in quantum efficiency in the range of about 7 eV to 100 eV photon energy is due to absorption and reflection by the entrance SiO_2 window.

With 100 % quantum efficiency the radiation energy is integrally converted to an electric current almost attaining a responsitivity of $\eta = 1/3.65$ eV $= 0.274$ A/W. Figure 3.4 shows the responsitivity of the photodiodes to photons, electrons and hydrogen ions. The experimental data has been obtained using a AXUV100G array, but it is representative for the whole AXUV-series of photodetectors. The data has been measured by NIST [X]. Again the influence of the SiO_2-layer is clearly visible and for energies greater than 200 eV the response is almost flat (the flat part occupies almost the whole spectrum, the figure plots the responsitivity against logarithmic scale). This flat power response results in the application of AXUV-detectors on several tokamaks for radiated power measurements over a wide-range of energies.

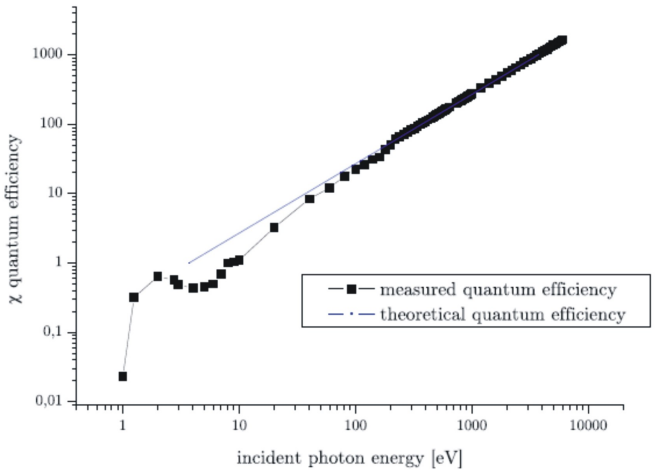

Figure 3.3: *Quantum efficiency χ of the AXUV-detector. Experimental data delivered by the manufacturer [17]. The blue line shows theoretical quantum efficiency.*

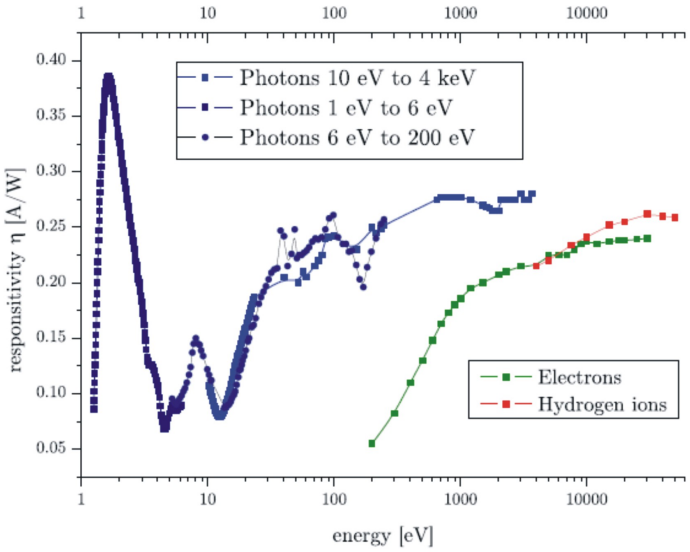

Figure 3.4: *Typical responsitivity η of the AXUV photodiodes to photons, electrons and hydrogen ions. The experimental data has been established by the NIST and was obtained from the manufacturer [17].*

An important question is the stability of the quantum efficiency when irradiating the detector with high doses of UV. The interface between Si and SiO_2 is susceptible to UV radiation. UV may neutralize the oxide charge which leads to a smaller electric field and resulting in a lower photocurrent (observed at high wavelengths). High baking temperatures may lead to a change of the oxide layer thickness leading to lower quantum efficiencies. Another reason are dislocations near the same interface due to environmental stress which may release recombination of the electron-hole pairs. The stability guaranted by the manufacturer is shown in figure 3.5.

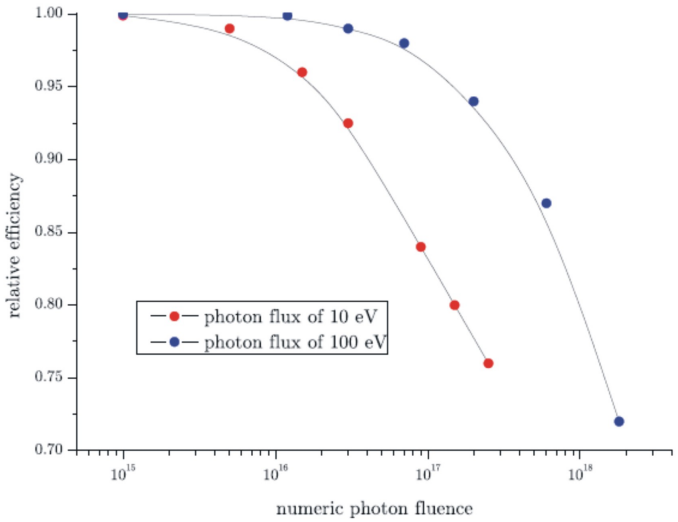

Figure 3.5: *Stability of the quantum efficiency of AXUV-photodetectors. A flux of* 5×10^{13} *photons* $s^{-1}.cm^{-2}$ *at 10 eV (red) and of* 3×10^{14} *photons* $s^{-1}.cm^{-2}$ *at 100 eV (blue) have been used. Data delivered from the manufacturer [17].*

Next factor which may influence the stability is the deposition of thin films on the surface of the detector, which leads to increasing thickness of entrance window and may vary the detection efficiency.

In comparison with metal foil bolometers AXUV-detectors exhibit a short nominal rise time of the order of the μs which gives access to observation of fast phenomena like MHD-activity or other types of instabilities. Also the high sensitivity allows making the active surface relatively small (in order of mm) what is the prerequisite for the measurement with high spatial resolution.

Unlike the thermal bolometers, AXUV detectors don't measure neutral particles of lower energy ($\leq$ 500 eV). This fact can be used to determine the power carried

by neutral particles by calculating the difference between the signals of both types of bolometer [18].

Table 3.1 summarizes the properties of resistive and AXUV bolometers.

Detector type	**Resistive bolometer**	**AXUV photodiode**
NEPD	$60\mu W cm^{-2}$	$60nW cm^{-2}$
(optimal)	$1\mu W cm^{-2}$	-
100USD/ch	60-120	6-12
Δ t	1ms	1μs
Vacuum feed	5 wires/ch	1 wire/ch
Compact	4ch - 2x3cm	20ch - 1x3cm
Merit	Abs. calibration	No neutrals $\leq$10keV

Table 3.1: *Comparison of bolometer detector types. NEPD - noise equivalent power density*

3.1.3 Bolometers for COMPASS

As mentioned in introduction, the principal aim of bolometric diagnostic on COMPASS will be observation of fast processes in plasma. Therefore the main arguments were the temporal and also spatial resolution, thus the AXUV diodes were choosed. Work experience with AXUV's on older Prague tokamak CASTOR was next strong argument.

The used detectors AXUV20ELM were manufactured by International Radiation Detectors Inc. It consist of 20 silicon photodiodes, which are mounted on a planar chip (fig. 3.2 and fig. 3.6). The chip is shipped with ceramic socket for fixation and insulation (fig. 3.2). The detectors are intended for measurement of absolute radiation in spectral range from ultraviolet (UV) up to soft X-ray radiation. It means photons with energy 7eV-6keV (i.e. wavelengths from 0,2nm to 180nm). The AXUV20ELM

Lenght of active area	18.8mm (20 channels)
Lenght of single diode	0.75mm
Width of single diode	3.7mm
Distance between diodes	0.14mm
Area of single diode	$3.78mm^2$

Table 3.2: *AXUV20ELM detector array dimensions*

diodes are connected in conducting direction, thus they are operating like simply current generators. In table 3.2 dimensions of AXUV20ELM detector are summarized.

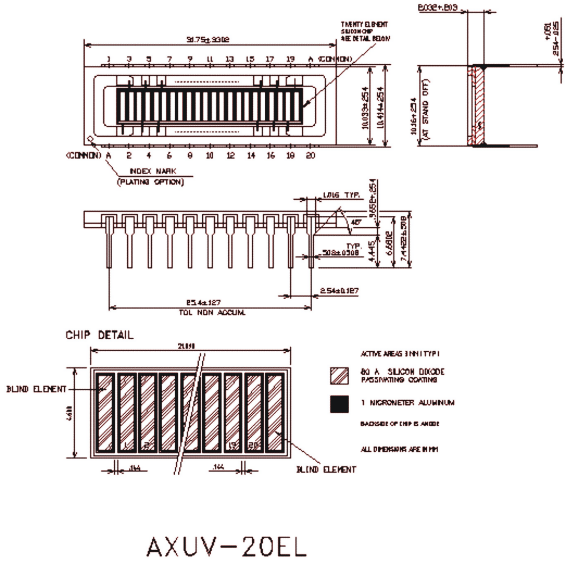

Figure 3.6: *Scheme of AXUV20ELM detector [16]*

3.2 SXR detectors

Similar requirements as on bolometers were imposed by selection of SXR detectors [15]. In this case primarily experiences of other experiments were taken into account . The SXR measurements on JET [19] and ASDEX [20] tokamaks are successfully performed using the photodiodes array LD 35-5T (JET) WINDOWLESS manufactured by Centronic Ltd (Fig 3.7). The same detectors were chosen for measurements on COMPASS tokamak.

The operation principle of these SXR detectors is completely the same as by AXUV detectors - the inner photo effect. But in contrast to AXUV's the SXR photodiodes are connected in reverse direction. Thus the efficiency of the diode measurement depends on the depletion layer depth, which can be increased when a reverse bias voltage is applied. The problems of signal handling will be closely discussed in the next chapter.

The detector array LD 35-5T (JET) WINDOWLESS is composed of 35 silicon photodiodes [21], which are linearly ordered (fig 3.7). Also this chip is shipped with

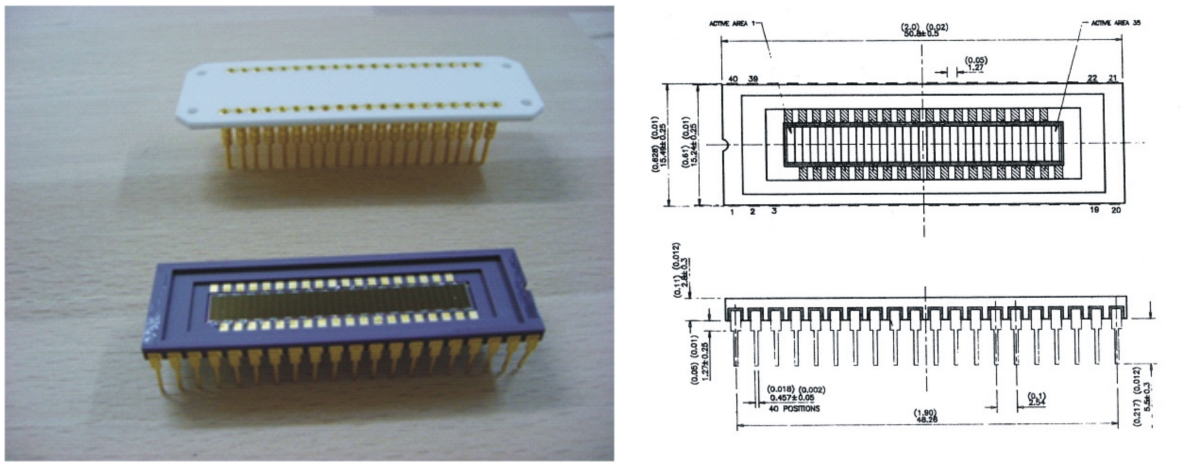

Figure 3.7: *Photo of LD 35-5T (JET) WINDOWLESS (left), scheme of this detector (right)[21]*

ceramic socket, which had to be reduced because of large area of ceramic plate in original version (see fig. 3.7). The diodes, which may also be used as sensors in the visible range, are sensitive to a large part of the electromagnetic spectrum. A filter will be used to select the SXR range. That will be done by placing a beryllium foil in front of the detector. On COMPASS a flat foil with a thickness of 5.1 μm will be used, which results in high-pass filtering at 0.5 keV (design details in next chapter 4). The detector itself is sensitive to this radiation, but its sensitivity starts to fall off above about 8 keV. In fact this way modified detectors provide reasonable measurement of radiation in region from 0.5keV to 10keV (i.e. wavelengths from 0.125 nm to 2.5 nm).

Lenght of active area	34.6mm (35 channels)
Lenght of single diode	0.96mm
Width of single diode	4.6mm
Distance between diodes	0.03mm
Area of single diode	$4.42mm^2$

Table 3.3: *LD 35-5T (JET) WINDOWLESS detector array dimensions*

In table 3.3 dimension of SXR detector are summarized. Fig. 3.8 and fig. 3.9 show calculated quantum efficiency and relative efficiency of detection using detector with 5.1μm thick beryllium foil.

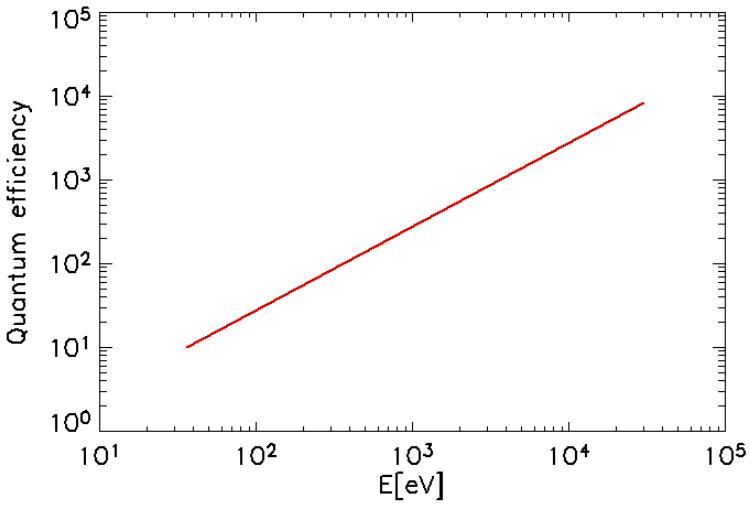

Figure 3.8: *Calculated quantum efficiency of LD 35-5T (JET) WINDOWLESS detector*

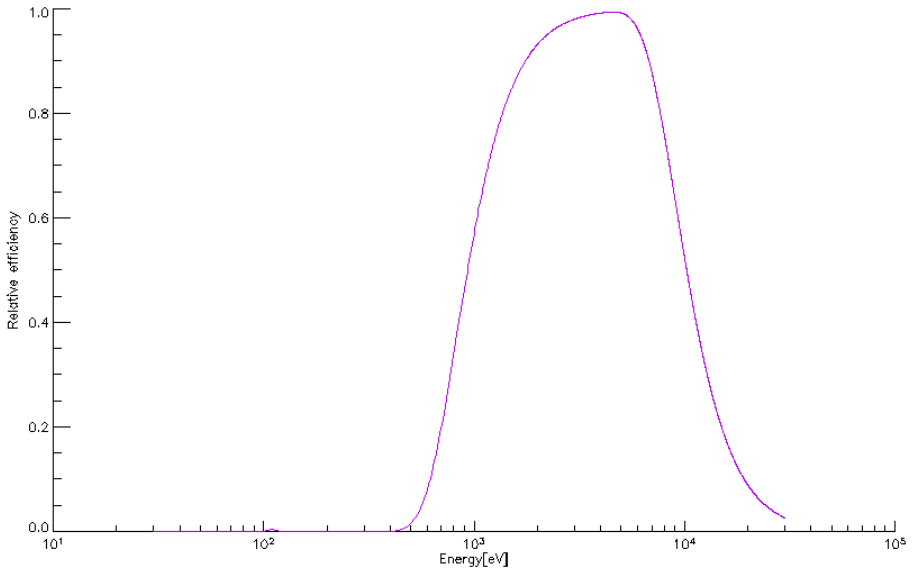

Figure 3.9: *Calculated relative efficiency of detection of LD 35-5T (JET) WINDOWLESS detector with 5.1μm Be foil*

3.3 Camera obscura

The main objective of bolometry and SXR diagnostic on COMPASS is to monitor a distribution of radiated power and namely to observe fast radiating events connected with plasma instabilities. These measurements require a high temporal resolution, but also good spatial resolution. The photodiodes detect photons incoming from the whole plasma thus in general they don't have spatial resolution. But we want to achieve situation that each diode detects photons from other part of the plasma.

Assuming a strong toroidal symmetry (along the torus), a complexity of the problem can be simplified to 2D observations in a poloidal cross-section of the tokamak plasma (circular or D-shape).

For the measurements the principle of camera obscura is used [22]. That means the detector array is closed in tight case, where photons pass only through a narrow pinhole. In fig. 3.10 it is illustrated that every detector reads out the other part of the plasma and measures the radiation from the field of view according to its direction. Optimizing the width of pinhole and its distance to detector it is possible to reach a full coverage of plasma and minimize the overlap of neighbouring channels, which improves information about spatial distribution of plasma radiation. Calculation of these parameters is discussed in next chapter.

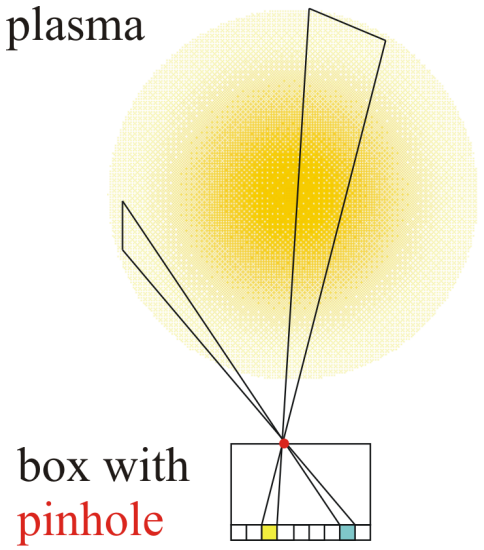

Figure 3.10: *Principle of camera obscura*

Indeed these measurements do not provide information on local properties; they are integrated along the chord, i.e. originate from a whole solid angle of the detection. But these data can be processed using special transformations to get local radiation. These procedures are described in chapter 5.

Chapter 4

Design of detection system

For purposes of bolometric and SXR diagnostics together with visible light spectroscopy (VIS) four diagnostic ports at the same poloidal cross-section in the sector 6/7 of the COMPASS tokamak (see Fig. 4.1) were assigned. Unfortunately, all ports are very small, what is a general limitation of the COMPASS tokamak. In the first phase of system development a situation of the angular upper port was solved (inner diameter 97mm).

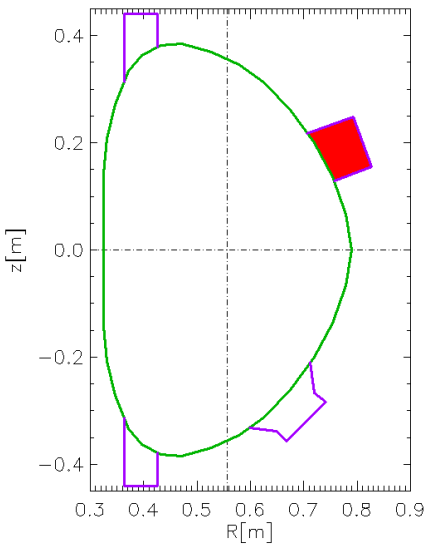

Figure 4.1: *Poloidal cut of section 6/7, the green oval shows the vacuum chamber and the violet rectangles indicate the diagnostic ports (angular upper port accentuated).*

At the beginning, the crucial question was which and how many detectors can fit into constrained space of the diagnostic port. Simultaneously it had to be taken into account the necessity of the shutter to prevent detectors and optics (VIS) from an impurity layers deposition during cleaning glow discharge, an internal cooling to prevent detectors from overheating during vacuum vessel baking and thermocouples for temperature monitoring.

Using simple geometry considerations and taking into account requirements of each diagnostic it was decided to install inside the angular upper port two arrays of the AXUV bolometers, one SXR detector and optical system for VIS diagnostic.

4.1 Observation angles

Before the development of the inside port plug incorporating detector holder, setup of camera obscura had to be established. The goal of the arrangement is to cover the whole plasma in case of AXUV's with the best possible space resolution and reach the best possible covering of central plasma in case of SXR detectors. The same method was used for setup calculations for AXUV and SXR detectors. It will be demonstrated on case of one AXUV detector.

The crucial role of the detection system effectiveness plays its setup. In this section we will calculate one AXUV detector space arrangement from conditions given by tokamak, port and plasma positions. We will discuss three simple approximation steps used for evaluation [4].

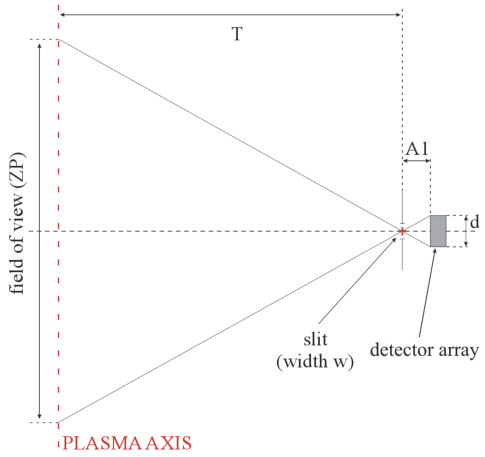

Figure 4.2: *Detection system setup*

As initial conditions we consider the distance between the slit and the vertical plasma axis (the centre of plasma) T, the length of the detector array d, length of each single detector sd, distance between detectors ds, the field of view in the centre of plasma ZP and the width of the slit w.

In the first approximation we consider the slit as a punctual object, which means the width of the slit decreases to zero ($w \rightarrow 0$). Than we can calculate ideal distance between the slit and the detector array A1 using the method of similar triangles (see fig. 4.2). We can write:

$$\frac{\frac{ZP}{2}}{T} = \frac{\frac{d}{2}}{A1} \tag{4.1}$$

This equation can be simply retyped as dependence for $A1$ and establish value of the distance between detector and slit as:

$$A1 = \frac{d.T}{ZP} \tag{4.2}$$

For evaluation of the single detector space resolution for central channel PR we use analogous geometrical construction as in previous step only with three similar triangles (see fig. 4.3), but further we consider a real slit size $w \neq 0$. We can write:

$$\frac{\frac{w}{2}}{A1s} = \frac{\frac{PR}{2}}{T + A1s} \quad and \quad \frac{\frac{sd}{2}}{A1 - A1s} = \frac{\frac{PR}{2}}{T + A1s} \tag{4.3}$$

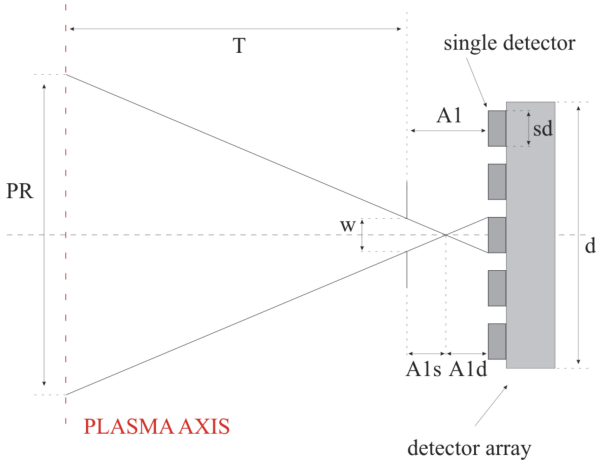

Figure 4.3: *Illustration of the single detector space resolution*

From the first equation we express A1s as:

$$A1s = \frac{\frac{w}{PR}T}{1 - \frac{w}{PR}} \tag{4.4}$$

and then substitute A1s by this expression in the second equation. Finally we get relation for PR:

$$PR = w + \frac{T}{A1}(sd + w) \tag{4.5}$$

Next important parameter, which we want to minimize, is overlap of neighbouring detectors PRS. Value of this parameter can be calculated as distinction of the single detector space resolution in the middle of plasma PR and the distance between mid-points of neighbouring detectors field of views Δ (see fig. 4.4). We apply the method of similar triangles again:

$$\frac{\Delta}{T} = \frac{sd + ds}{A1} \tag{4.6}$$

thus

$$PRS = T\frac{sd + ds}{A1} - PR \tag{4.7}$$

Because we want to cover the whole plasma but we won't measure twice the same signal (so called cross-talk), it is suitable to keep overlap near zero.

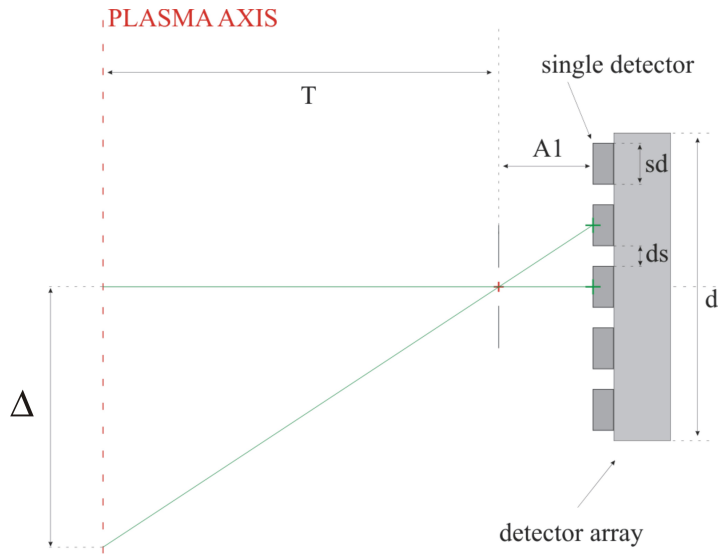

Figure 4.4: *Illustration of overlap calculation procedure*

Appearing from these calculations, the IDL procedure was written to optimize the parameters and visualize the resulting "fans" of view. Variables of this procedure are directly related to port plug dimensions in order to prohibit physically impossible alignments. They are vertical shift of detector against port axis S, vertical shift of pinhole against detector centre SP, distance between detector and pinhole $A1$, and pinhole width w (See fig. 4.5).

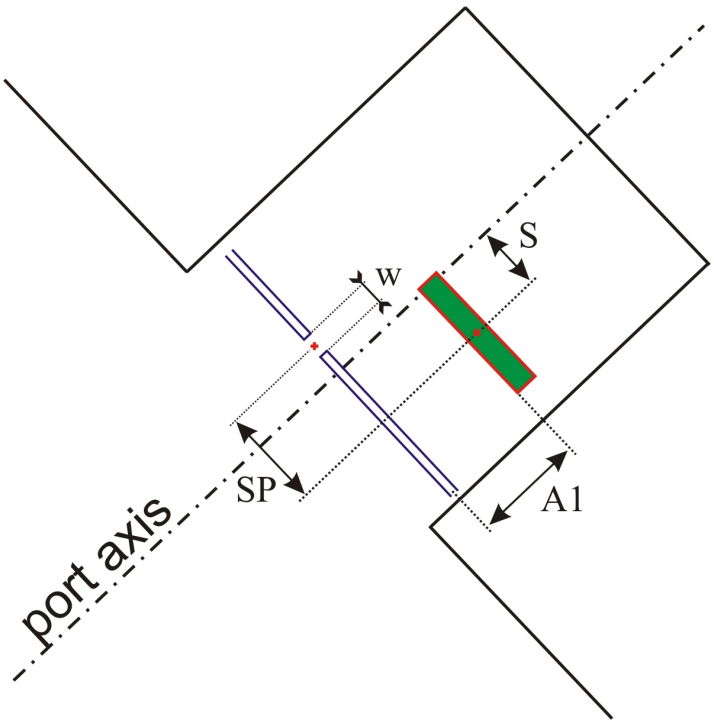

Figure 4.5: *Diagnostic port poloidal cut with shown variables of optimizing process, the green rectangle marks the detector and blue lines the pinhole*

These values were optimized for maximal plasma covering with reasonable spatial resolution. The resulting parameters are summarized in table 4.1 and the fans of view are shown in fig 4.6.

As visible on fig. 4.6, AXUV 1 detector array is intended for observation of lower part of plasma and AXUV 2 array for upper part of plasma, thus they cover the whole plasma profile. The SXR detector is focused on the centre of plasma column.

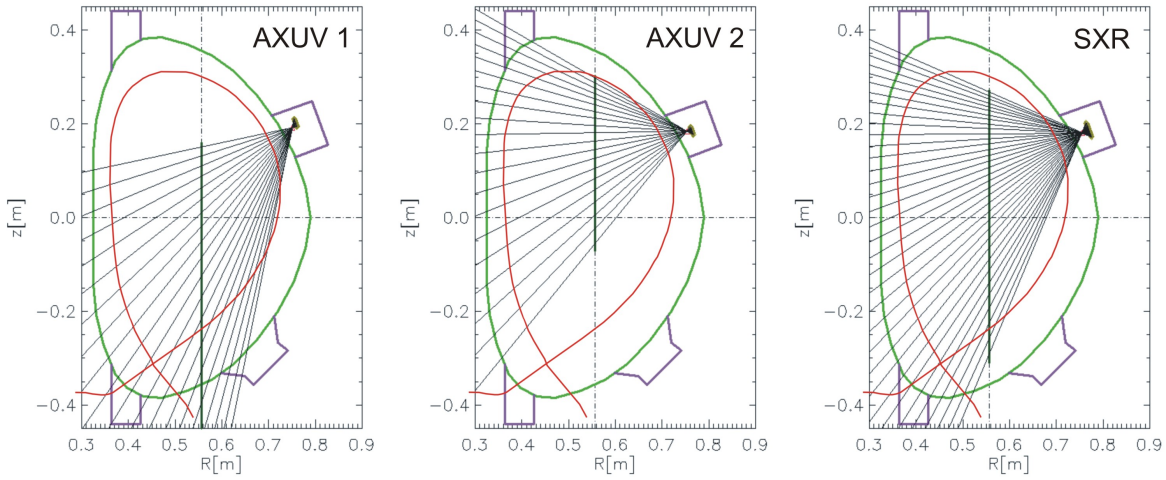

Figure 4.6: *The coverage of the poloidal cross-section by the detectors of AXUV 1 (left), AXUV 2 (middle) and SXR (right). The red curve visualizes a probable plasma shape.*

	AXUV1	**AXUV2**	**SXR**
Pinhole width	100μm	100μm	100μm
Vertical shift of detector against port axis	+18.5mm	0mm	0mm
Vertical shift of pinhole against detector	-7.5mm	+3mm	-1mm
Distance between detector and pinhole	10mm	10mm	16mm
Field of view on vertical plasma axis	[-839,+160]mm	[-72,+303]mm	[-310,+271]mm
Spatial resolution on the vertical plasma axis	18.0mm	21.1mm	16.6mm
Overlap	-3.8%	-3.9%	-0.3%
Depth of shutter in port	60mm	60mm	60mm

Table 4.1: *Final setup parameters of AXUV's and SXR detectors*

4.2 Port plug

Considering the calculated alignment of particular components, a basic design was developed according to the demand to integrate all above-mentioned spectroscopic systems with both the cooling and the shutter in the limited port area. Therefore, this port plug is assembled from two pieces. The first is an inset which holds detector sockets with detectors, air slits, shutter, thermocouples and also includes a cooling channel (fig. 4.7). The second piece is the NW100 flange with electric feedtroughs and holes for VIS [23] and shutter (fig. 4.8) [24].

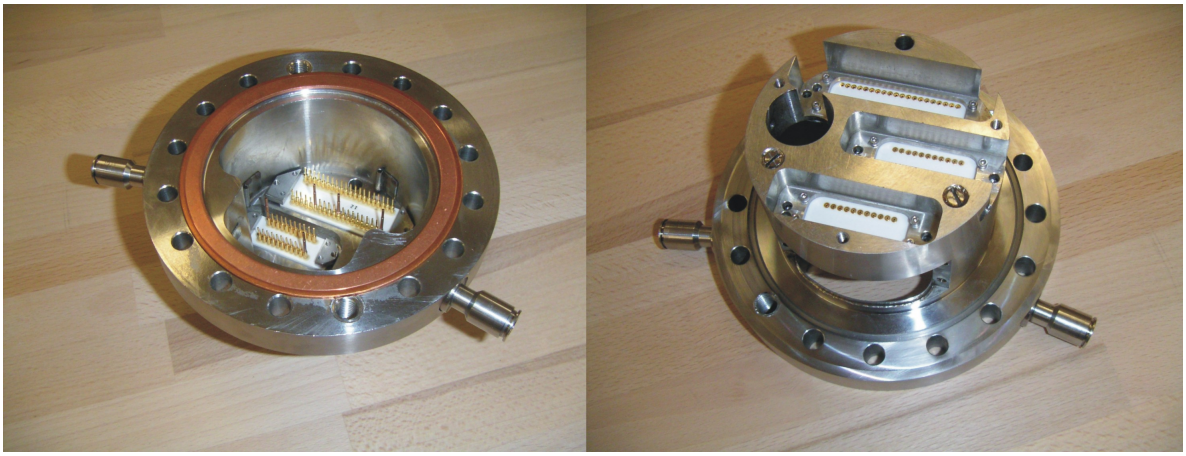

Figure 4.7: *Photo of the first part of port plug with mounted detector sockets, air side (left) and vacuum side (right)*

The inset design was developed from a placement scheme of detectors with regards to required observation angles and need of retaining the alternative of easy assemblage of the whole port plug. At the beginning, there were two possible ways of designing a part holding detectors. The first one was to make a separate case for each detector. This option is advantageous in a relatively simple construction and easy connection between detectors and electrical feedthroughs. However, it would be complicated to connect the cooling to more than one case inside a limited port area. The other option was to make a detectors holder as one monolithic inset. This inset is difficult to manufacture, but it has the advantage of compactness. Therefore, this option was chosen. In this case, the cooling channel is drilled through the inset, and holes on the vacuum side are sealed by threaded stoppers and welded. The next requirement was to assemble the whole diagnostic port plug "on the table," before the final connection to the tokamak. These

requirements were succeeded by sandwich structure of inset, which contains input and output of the cooling channel, allows assembling the port plug to the tokamak flange and also is used to connect the NW100 flange to the inset.

The NW100 flange contains two electrical feedthroughs, each equipped with 41 pins, one hole for a rotary feedthrough (NW16 flange) intended as a shutter manipulator, and the second hole for the NW35 viewport. The first feedthrough is assigned to signals from AXUV detectors and the second to SXR detector and two thermocouples. The NW35 vacuum window is made of fused silica and is used by VIS diagnostics. Position of the rotary feedthrough (NW16 flange) is given by a free area left on the inset in connection with a placement of the electrical feedthroughs, which should be located close to the detector sockets to simplify their cabelling.

Figure 4.8: *Photo of the first part of port plug with mounted detector sockets, air side (left) and vacuum side (right)*

As mentioned, thanks to the complex structure of the inset, detector sockets for bolometric and soft X-ray measurements and thermocouples could be connected to the electrical feedthroughs before a final assemblage of the inset and the NW100 flange (fig. 4.9). These connections between socket pins and pins on electrical feedtroughs were made with silver wire (diameter 0.25mm) with kapton insulation and silver shielding. Unfortunately, the crimp intended for sticking on pins are too wide (socket crimps

0.81mm diameter, feedthrough pins 1mm diameter) for usual fasten with pliers. Therefore, the wire had to be soldered into crimps with a special high temperature solder (221°C) using mixture of 96% of tin and 3.5% of silver as soldering material without additions of other usual components like lead, cadmium or zinc. Also use of special soldering flux was required. Shielding of all wires was soldered together to the common ground of corresponding detector and this bundle of wires was subsequently winded around with wire carrying this ground. In order to prevent mixing signals between pins, they are placed in a vespel spacer on side of vacuum feedtrough. On the second side, the connection was insulated by a kapton tape (see fig. 4.9). It is also necessary to ensure the insulation between wires and the body of the port plug, because the eventual connection can strongly affect the measurement and can damage the amplifiers, which will be descibed further. According to this experience, a purchase of new high-vacuum cables is planned to simplify a physical realization of the socket-feedthrough connection.

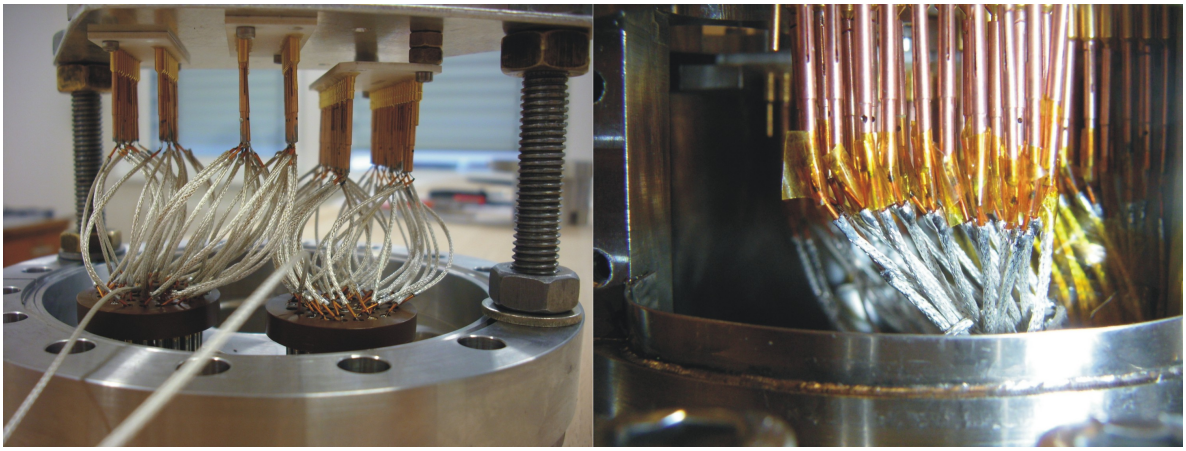

Figure 4.9: *Photo of inside vacuum connections between electrical feedthroughs and detector sockets (left) and detail of kapton insulation of crimps on socket side (right)*

After on air compounding, the NW100 flange was bolted to the port plug and sockets were bolted to the inset through a mounting hole. The mounting hole was closed subsequently. Afterwards, detectors were mounted from the front side and covered by an air slit holder (fig. 4.10). The air slit holder is used for movement of the slit against the detector centre, if a change of observation angle is required.

As a collimating element for the bolometers and a soft X-ray detector, the 0.1mm wide (calculated above) and 2mm long air slit together with the second, exactly the

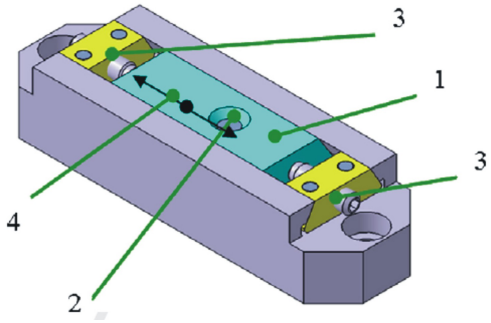

Figure 4.10: *Air slit holder (1-gliding stone, 2-air slit, 3-fly screw, 4-movement of gliding stone)*

same air slit in a perpendicular direction were used. The air slits are replaceable, what allows an independent change of the vertical and toroidal spatial resolutions by the modification of air slit width. Changing the toroidal resolution, mainly the throughput will be influenced due to a toroidal symmetry of observed plasma. In case of soft X-rays, a thin beryllium foil (5.1 μm) is used to filter VIS and UV radiation. To prevent air slits and foil from rupturing during a chamber pumping or refilling, pressure relieve holes were added into the inset.

The cut through the port plug and the final design of the assembled diagnostic port are shown in fig. 4.11 and fig. 4.12. Figure 4.13 schematically illustrates the distribution of the mentioned components inside port from the upprer view.

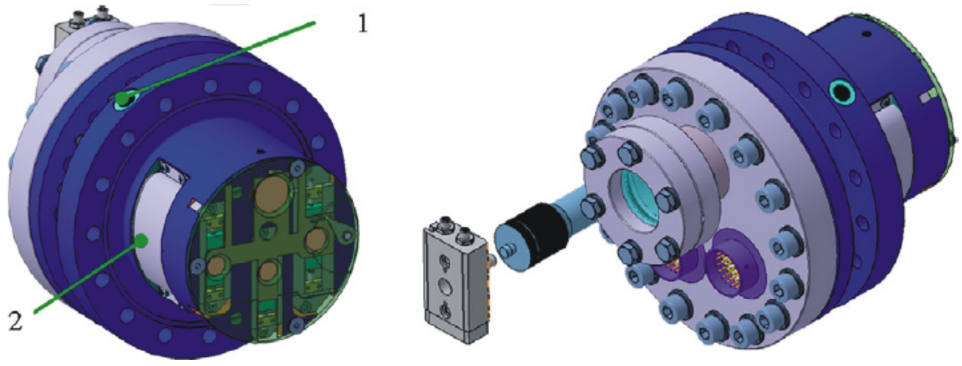

Figure 4.11: *3D view of the assembled port (vacuum side-left picture, atmospheric side-right picture, 1-cooling channel inlet, 2-mounting hole).*

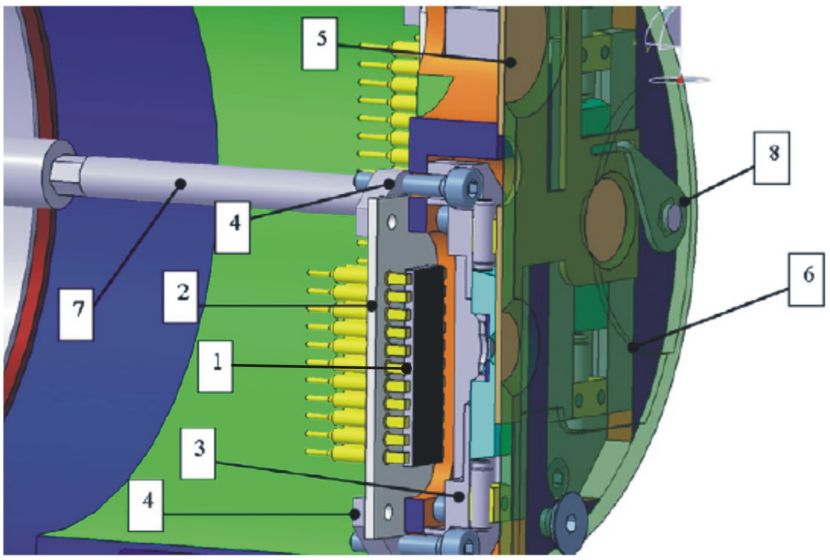

Figure 4.12: *Port cut through (1-detector, 2-detector socket, 3-air slit holder, 4-nut, 5-shutter, 6-hood (holds the shutter), 7-connection shaft (link shutter jack and rotary feedthrough), 8-shutter jack)*

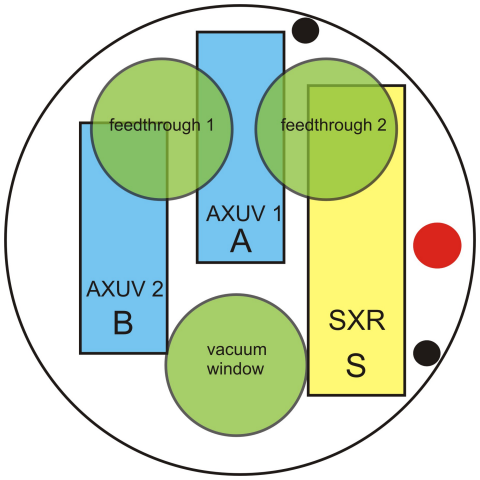

Figure 4.13: *Illustration of distribution of components inside port - upper view (black circles indicate thermocouples, red circle shutter manipulator hole)*

4.3 Amplifiers

The output current from photodetectors is typically very small, less than 0,1μA. In order to perform effective measurement, it is necessary to amplify the measured current and convert it to voltage as the data acquisition system requires. For these purposes special low-noise multi-channel amplifiers were developed. This section discusses design and tests of these amplifiers.

4.3.1 Amplifier design

Because of small currents generated in photodiodes, it is necessary to amplify them as close to detectors as possible. The amplifiers are usually located directly behind the detectors still inside vacuum. Unfortunately, this solution can't be applied in case of the COMPASS tokamak, due to limited space inside diagnostic ports. Thus, the amplifiers are connected straight on air side of vacuum feedtrough.

Two prototypes of boxes of amplifiers with signal input optimized as counterpart for the air side of vacuum feedthrough were proposed. These boxes always take care for all signals from the feedthrough. The first one cares for signals originating from two AXUV detectors (feedthrough 1) and the second handles SXR detector and thermocouples (feedtrough 2), where signal from thermocouples is only converted to voltage, not amplified.

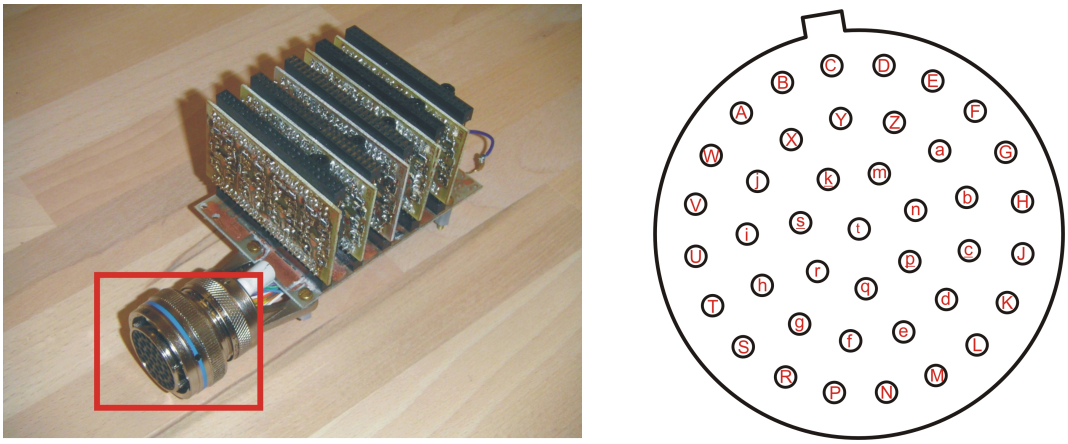

Figure 4.14: *Photo of final uncovered amplifiers box (counterpart connector to a vacuum feedthrough in red rectangle) - left, scheme of vacuum feedtrough with marked pins (air side) - right*

There is motherboard, which handles 5 rows each with 8 amplifiers (see fig. 4.14), inside of both boxes. In case of SXR motherboard, on the last row the thermocouples are also connected. Each box is powered by a specially developed source which energizes all amplifiers in the box and they also have a common ground. The SXR detector (photodiode) is connected in reverse direction and the measured signal has negative polarity, thus the offset 4.7V is applied as the simplest solution to reach the DAQ voltage range. AXUV photodiode is connected in conducting direction, so only 0.3V offset is applied. The biasing voltage used in a SXR case to extend a depletion layer (improve detector sensitivity) is also provided from amplifiers box.

Each amplifier has the two-stage structure. In the first stage, the measured current is transformed into voltage as:

$$\Delta U_{out} = I_{in} R_1 \tag{4.8}$$

In the second stage this voltage is amplified by factor:

$$A_u = 1 + \frac{R_2}{R_3} \tag{4.9}$$

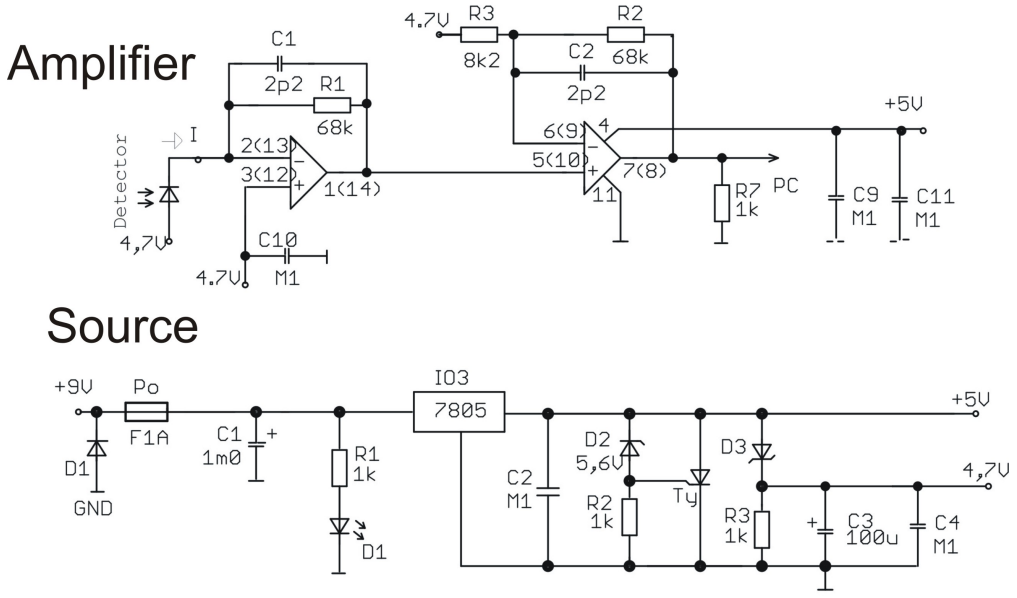

Figure 4.15: *Scheme of SXR amplifier and its source*

The final design of amplifiers was established after a laboratory test of time constants and offsets described below. The rate between input current and output voltage was

chosen as 6.3×10^5 for SXR amplifier and 5.2×10^5 for AXUV's amplifier (and can be changed according to future experimental needs). The bandwidth of both amplifiers was established as 1MHz. For higher frequencies amplification decreases linearly 6dB/oct. Schemes of amplifiers and appropriate power sources with all details are shown in fig. 4.15 and fig.4.16.

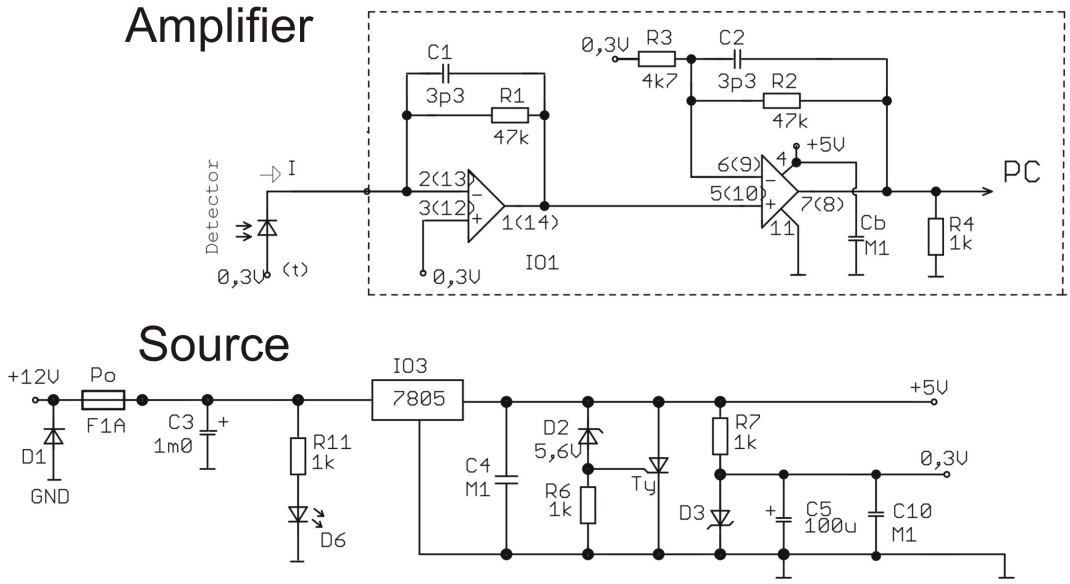

Figure 4.16: *Scheme of AXUV's amplifier and its source*

The signal from amplifier boxes is then guided by double-shielded cable (SSTP CAT.6 - wire strand) consisting of four twisted-pair wires. The structure of wire strand provides possibility of later manipulation with cables. These cables handle signal 7.5m from the diagnostic port to the cable-junction box located under the tokamak. They are ended with RJ-45 conector and they are connected to a special wiring block, which is proposed to collect all cables from bolometric and SXR diagnostics. From this block the double-shielded cables consisting of four twisted-pair wires (SSTP CAT.7 - solid wire) handle the signal next 30m to the technologic room, where they are connected to CODAS (the COMPASS data acquisition system). Because the cables are intended for permanent placing, the solid wire structure is used. The schemes presented in fig. 4.17 and fig. 4.18 describe in detail the way of signal from detector to wirring block.

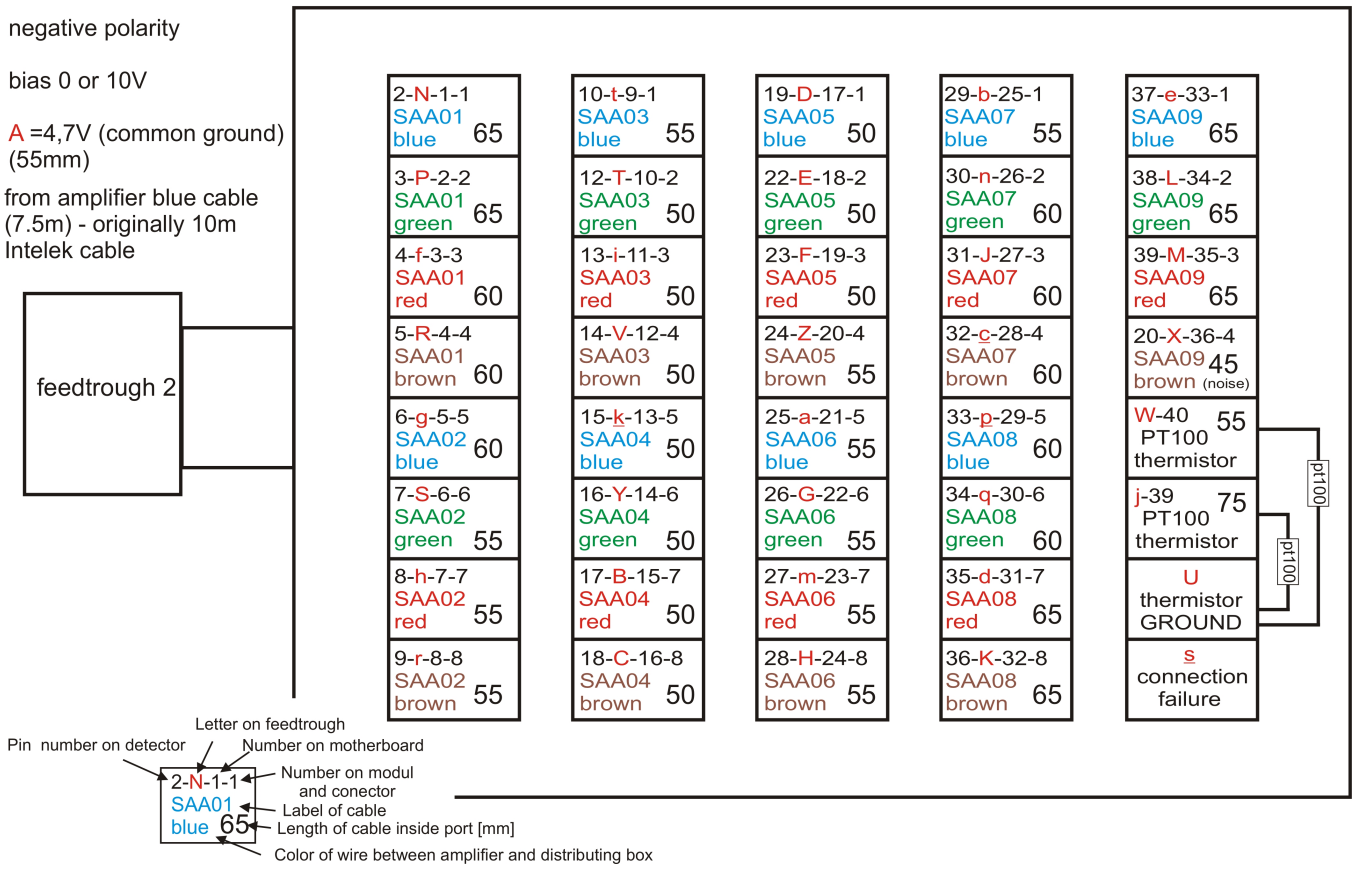

Figure 4.17: *Scheme of signal handling - SXR amplifier*

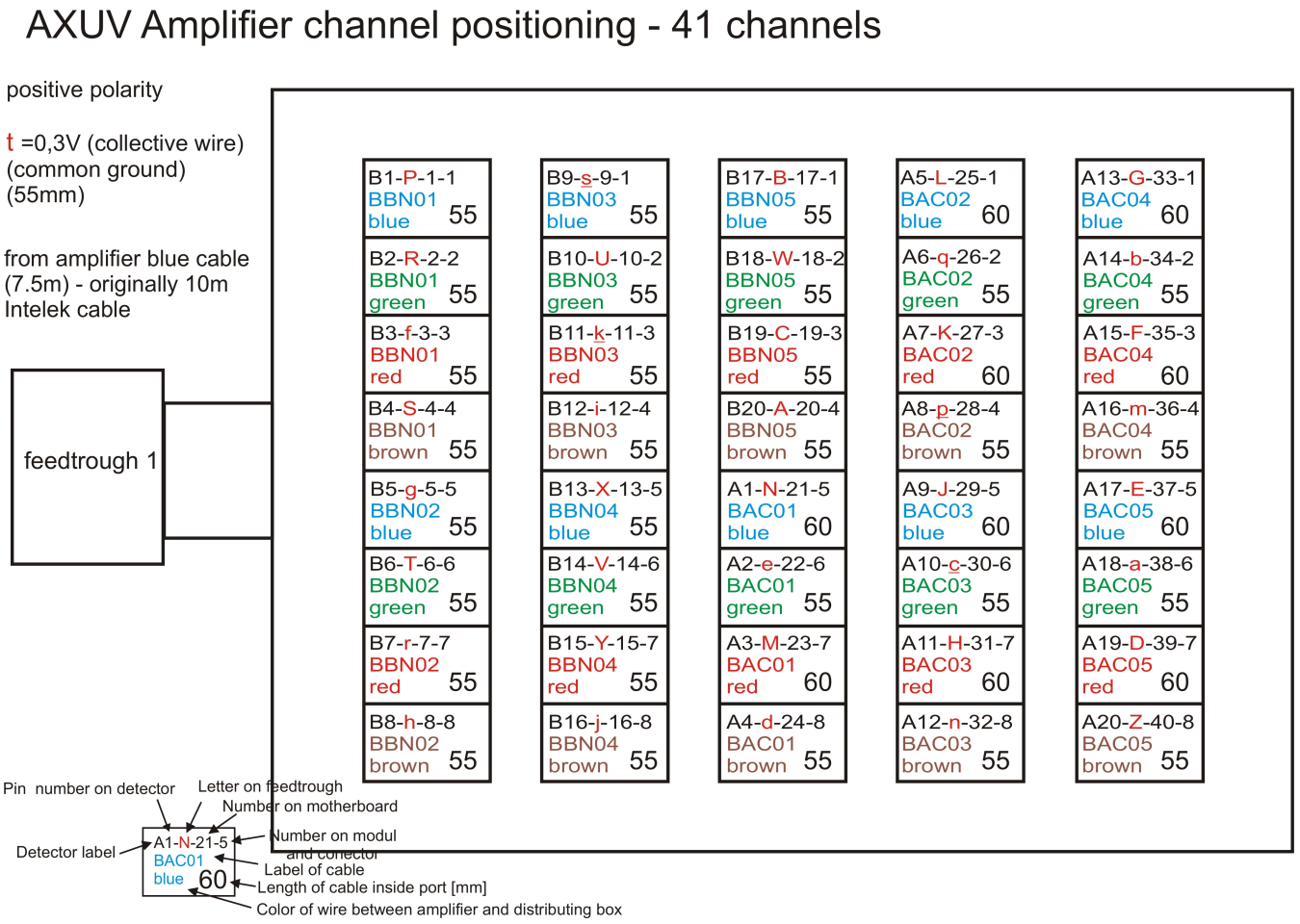

Figure 4.18: *Scheme of signal handling - AXUV's amplifier*

4.3.2 Amplifier tests

In order to measure characteristics of amplifiers and also to test functionality of detectors, prototypes of amplifiers applicable to simple laboratory measurements were constructed. This prototype enables to connect the detector directly to the amplifier. Output data were collected using an oscilloscope with sampling rate up to 0.02μs. The LED diode, energized by the pulse source, was used as a source of light for detectors and the shape of the diode signal was verified by a fast photomultiplier. Experimental setup is illustrated in fig.4.19.

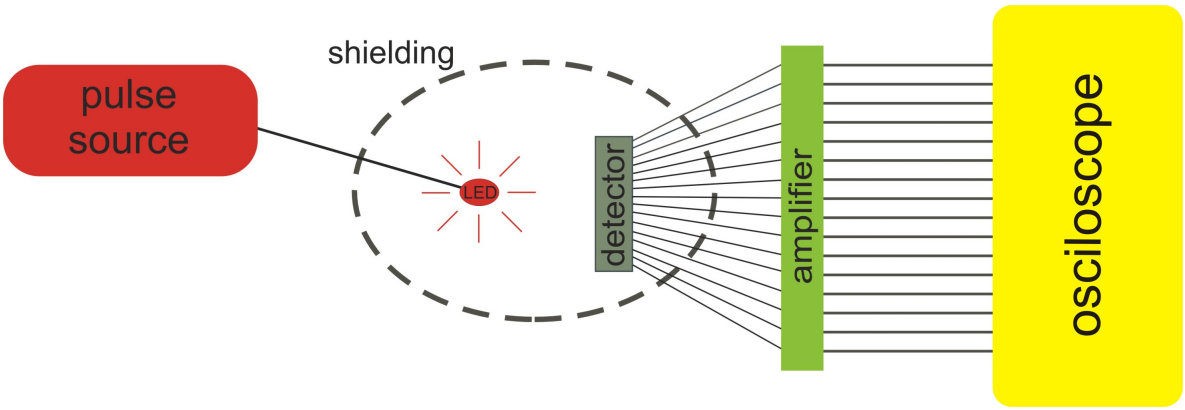

Figure 4.19: *Setup of test measurements*

The first set of measurements indicated that the time response of detector-amplifier system is longer than 1μs. In order to decrease the time constant the first channel of the amplifier was modified (resistance R_2 was decreased) and measurements were repeated. Results for modified channel reliably confirm the time constant below 1μs. Fig.4.20 shows fitted results for modified and unmodified channel. To get a time constant of the amplifier itself, measurement without detector was performed. By this measurement, the signal to amplifier was provided by the divider connected to the same pulse source as LED diode in previous measurements. This measurement confirms that the detector itself has only small (insignificant) influence to the value of time constant (See fig.4.20).

After modifying all channels, tests of typical response were performed, in sense of signal shape not magnitude. In the following, examples of AXUV and SXR detectors response for a wide spectrum of the pulse lengths are reported. Figures 4.21 and 4.22 show the source voltage of LED diode (5V pulse in figure decrased for better comparison) and the output voltage from the amplifier. In figures it is also ploted offset of detectors. In case of SXR amplifier it was used an offset of 2.5V, which was later incresed to 4.7V

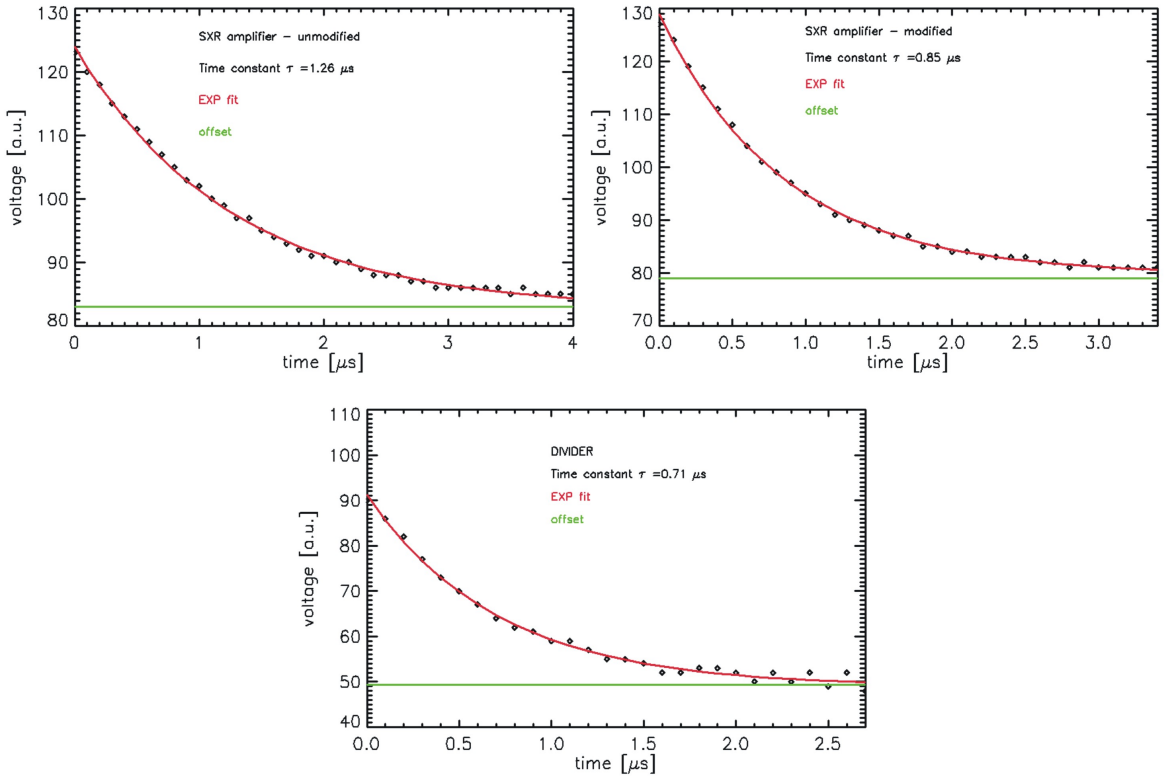

Figure 4.20: *Time constant exponential fit for SXR amplifier; modified channel results (up left), unmodified channel results (up right) and results for measurement without detector with modified channel (down)*

for a final version of amplifiers. The situation will be further improved with using new stabilized sources for amplifier boxes, which decrease the noise of detector offsets.

In detectors signals, there are visible oscilations following edges which cause that the system becomes in stacionary state aproximatelly after 5μs. This fact adversely affects the temporal resolution. It is caused by a finite bandwidth of amplifiers. It is limited by sampling rate of data aquisition system, which is 2MHz. That means, in sense of Nyquist–Shannon sampling theorem, the bandwidth of amplifiers can't exceed 1MHz.

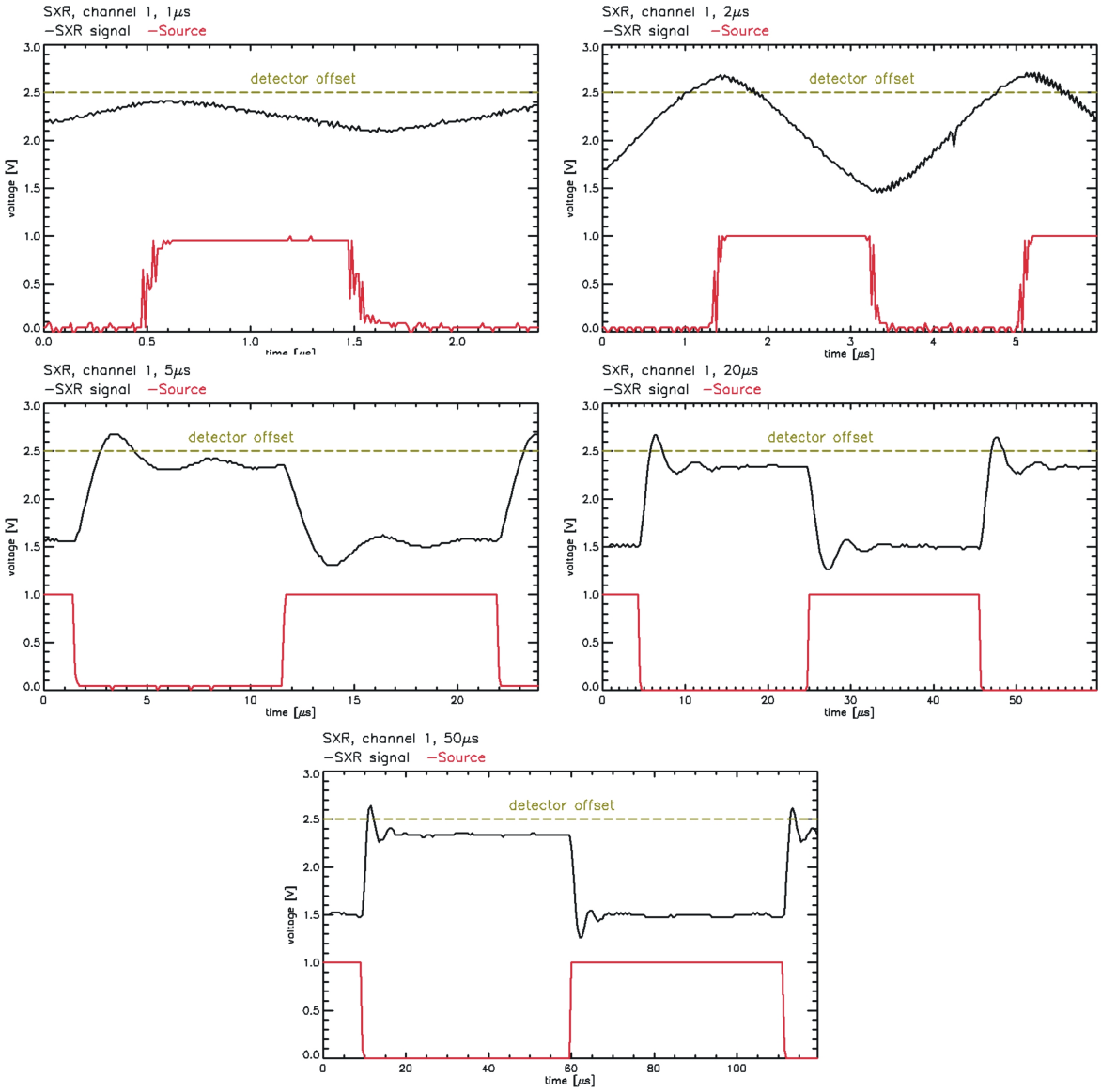

Figure 4.21: *Examples of characteristic SXR detector-amplifier system response for 1, 2, 5, 20 and 50μs pulse lengths. (red curve indicates shape of source voltage - 5V pulse, black detector-amplifier system response and green line offset of detector)*

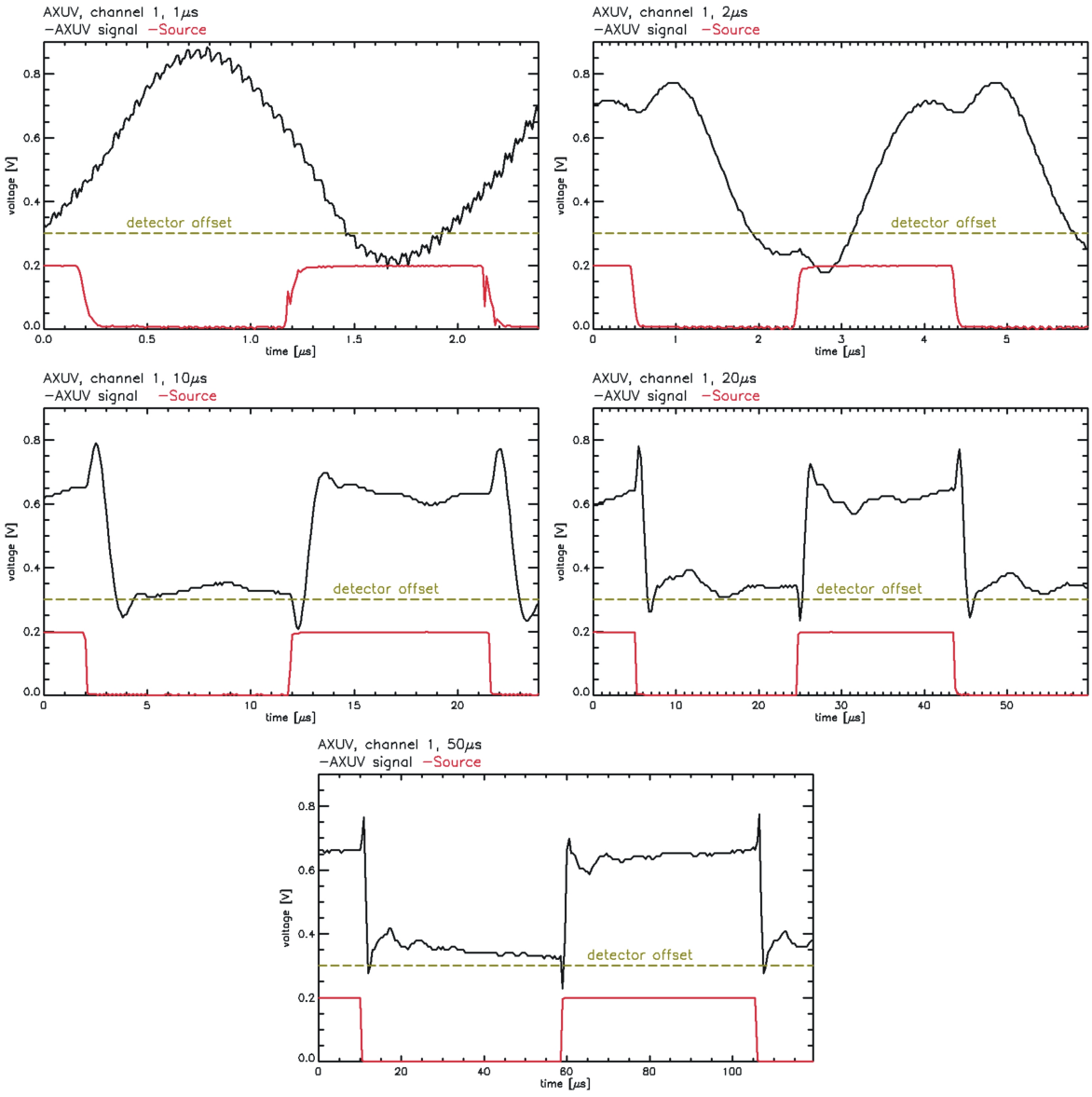

Figure 4.22: *Examples of characteristic AXUV detector-amplifier system response for 1, 5, 10, 20 and 50μs pulse lengths. (red curve indicates shape of source voltage - 5V pulse, black detector-amplifier system response and green line offset of detector)*

4.4 Relative calibration

To control fabrication-related spread of responsitivity and differences in amplification a relative calibration to weight the detectors response among each other was realized.

For this purposes the laboratory amplifiers were used. Initially a relative calibration of these amplifiers channels was done. The voltage source was stepwise connected directly to all amplifier channels and than the amplification of signal was measured. These values were subsequently normalized to 1 and used for next measurements. The results of relative calibration are shown in fig.4.23. The larger error bar of values in case of SXR amplifier is caused by a lower long-time stability of offset caused by a power source corresponding to a systematic error. That can be easily removed by a subtraction for short-time measurements, i.e. during a discharge of 1s. This noise will be partially suppressed with new stabilized power sources. For AXUV amplifiers the scatter is below 1%. However, the dispersion of mean values is 6% for SXR amplifier and 1% for AXUV.

In tables 4.2 and 4.3, the normalized correction factors for amplifiers channels are presented. By mutiplying signals by these factors, we reach the same amplification for all channels.

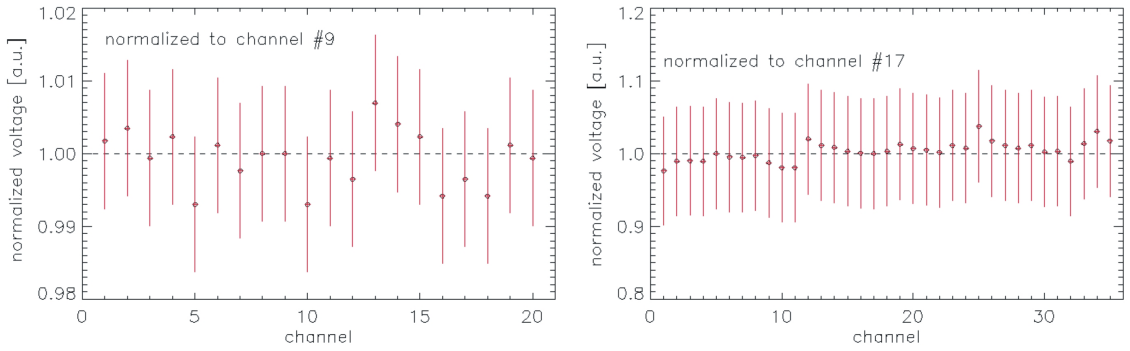

Figure 4.23: *Relative calibration for AXUV (left) and for SXR (right) amplifier channels normalized to 1*

The calibration of detectors has been done using a standard halogen lamp, assuming similar mutual ratios of the detectors sensitivity for visible range. However, this assumption is a strong simplification and recalibration using a soft X-ray source (radioactive Fe) is planned. Between detector and lamp there was located a scattering shade in order to reach the homogenous isotropic radiation (see fig 4.24). The scattering shade was

Channel #	**Corr. factor**	**Channel #**	**Corr. factor**	**Channel #**	**Corr. factor**	**Channel #**	**Corr. factor**
1	1.00	6	1.00	11	1.00	16	1.01
2	1.00	7	1.00	12	1.01	17	1.01
3	1.00	8	1.01	13	0.99	18	1.01
4	1.00	9	1.00	14	1.00	19	1.00
5	1.01	10	1.01	15	1.00	20	1.00

Table 4.2: *Results of relative calibration for AXUV amlifier channels - correction factors normalized to channel #9*

Channel #	**Corr. factor**	**Channel #**	**Corr. factor**	**Channel #**	**Corr. factor**	**Channel #**	**Corr. factor**
1	0.98	10	0.98	19	1.01	28	1.01
2	0.99	11	0.98	20	1.01	29	1.03
3	0.99	12	1.02	21	1.00	30	1.00
4	0.99	13	1.01	22	1.01	31	1.00
5	1.00	14	1.01	23	1.01	32	0.99
6	1.00	15	1.00	24	1.04	33	1.01
7	0.99	16	1.00	25	1.02	34	1.03
8	1.00	17	1.00	26	1.01	35	1.02
9	0.99	18	1.00	27	1.01		

Table 4.3: *Results of relative calibration for SXR amlifier channels - correction factors normalized to channel #17*

placed perpendicular to the detectors axis at distance of 20cm from detector. For data acquisition it was used an old PC system, which is cappable of reading out 32 channels with sampling rate 1MHz (32768 samples).

For each detector on detector array the mean value of measured signal from the whole 32768μs interval was calculated and then the relative calibration was done by comparing these values. Using this procedure all detectors were calibrated. That means four new SXR detector arrays, six new AXUV's and for comparison two old AXUV's which were before used for bolometric measurements on the CASTOR tokamak.

The influence of possible source anisotropy and misalignment was checked by measurements with detector rotated against the axis (cca 20°).

The results of relative calibrations are shown in fig. 4.25 fig. 4.26 and values of

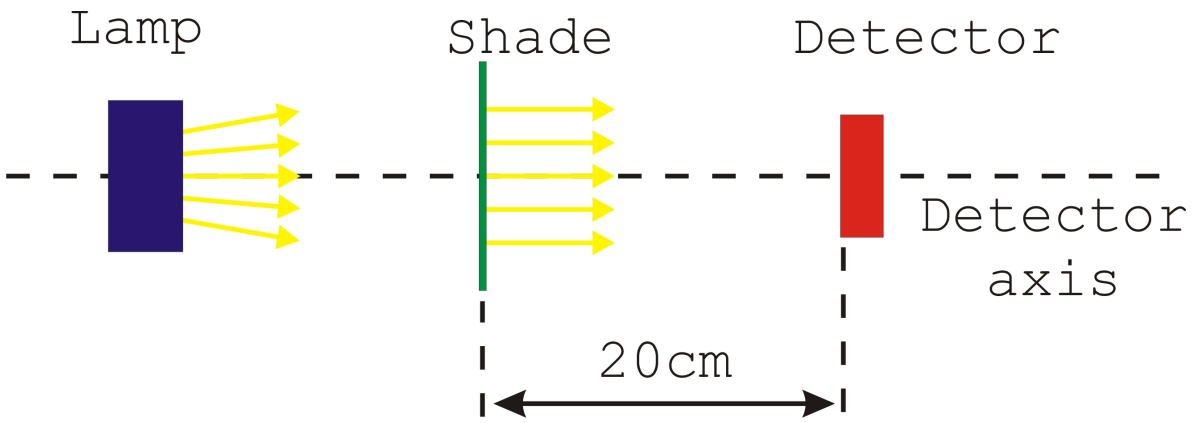

Figure 4.24: *Alignment of relative calibration measurements*

normalized correction factors are tabulated. In every plot the mean value of each diode response is shown and also maximal dispersion between them is accentuated. Diferencies between particular diodes on detector array for SXR detectors ranges from 5.9% for SXR2 up to 11.7% for SXR3. The situation with AXUV diodes is quite different. The dispersion of diodes response within array is significantly smaller. It ranges from 1.4% for AXUV26 to 3.2% for AXUV31. But this dispersion is valid only for 18 middle of 20 diodes. The first and the last diodes are shifted against others approximately by 50%.

From these figures it is also obvious a significant increase of dispersion by AXUV's, which were used on the CASTOR tokamak.

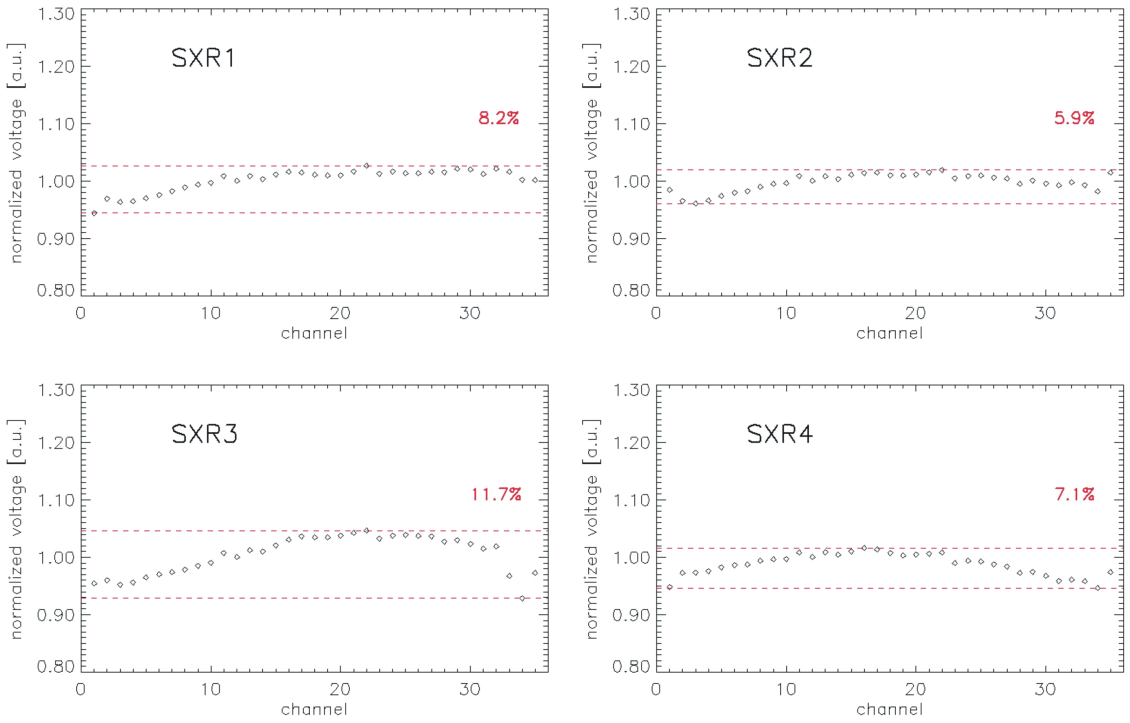

Figure 4.25: *Relative calibration of SXR detectors, red dashed lines indicate the maximal dispersion of values*

Channel #	**Corr. factor**	**Channel #**	**Corr. factor**	**Channel #**	**Corr. factor**	**Channel #**	**Corr. factor**
1	1.06	10	1.00	19	0.99	28	0.98
2	1.03	11	0.99	20	0.99	29	0.98
3	1.04	12	1.00	21	0.99	30	0.98
4	1.04	13	1.00	22	0.98	31	0.99
5	1.03	14	0.99	23	0.97	32	0.98
6	1.02	15	1.00	24	0.99	33	0.99
7	1.02	16	1.00	25	0.98	34	1.00
8	1.01	17	0.98	26	0.99	35	1.00
9	1.01	18	0.99	27	0.99		

Table 4.4: *Results of relative calibration for SXR 1 detector array channels - correction factors normalized to channel #12*

Channel #	**Corr. factor**	**Channel #**	**Corr. factor**	**Channel #**	**Corr. factor**	**Channel #**	**Corr. factor**
1	1.02	10	1.00	19	0.99	28	1.00
2	1.04	11	0.99	20	0.99	29	1.00
3	1.04	12	1.00	21	0.98	30	1.00
4	1.04	13	0.99	22	0.98	31	1.01
5	1.03	14	1.00	23	1.00	32	1.00
6	1.02	15	0.99	24	0.99	33	1.01
7	1.02	16	0.99	25	0.99	34	1.02
8	1.01	17	0.99	26	0.99	35	0.98
9	1.00	18	0.99	27	1.00		

Table 4.5: *Results of relative calibration for SXR 2 detector array channels - correction factors normalized to channel #12*

Channel #	**Corr. factor**	**Channel #**	**Corr. factor**	**Channel #**	**Corr. factor**	**Channel #**	**Corr. factor**
1	1.05	10	1.01	19	0.97	28	0.97
2	1.04	11	0.99	20	0.96	29	0.97
3	1.05	12	1.00	21	0.96	30	0.98
4	1.05	13	0.99	22	0.96	31	0.99
5	1.04	14	0.99	23	0.97	32	0.98
6	1.03	15	0.98	24	0.96	33	1.03
7	1.03	16	0.97	25	0.96	34	1.08
8	1.02	17	0.96	26	0.96	35	1.03
9	1.02	18	0.97	27	0.96		

Table 4.6: *Results of relative calibration for SXR 3 detector array channels - correction factors normalized to channel #12*

Channel #	**Corr. factor**	**Channel #**	**Corr. factor**	**Channel #**	**Corr. factor**	**Channel #**	**Corr. factor**
1	1.05	10	1.00	19	1.00	28	1.03
2	1.03	11	0.99	20	1.00	29	1.03
3	1.03	12	1.00	21	0.99	30	1.03
4	1.02	13	0.99	22	0.99	31	1.04
5	1.02	14	1.00	23	1.01	32	1.04
6	1.01	15	0.99	24	1.01	33	1.04
7	1.01	16	0.98	25	1.01	34	1.06
8	1.01	17	0.99	26	1.01	35	1.03
9	1.00	18	0.99	27	1.02		

Table 4.7: *Results of relative calibration for SXR 4 detector array channels - correction factors normalized to channel #12*

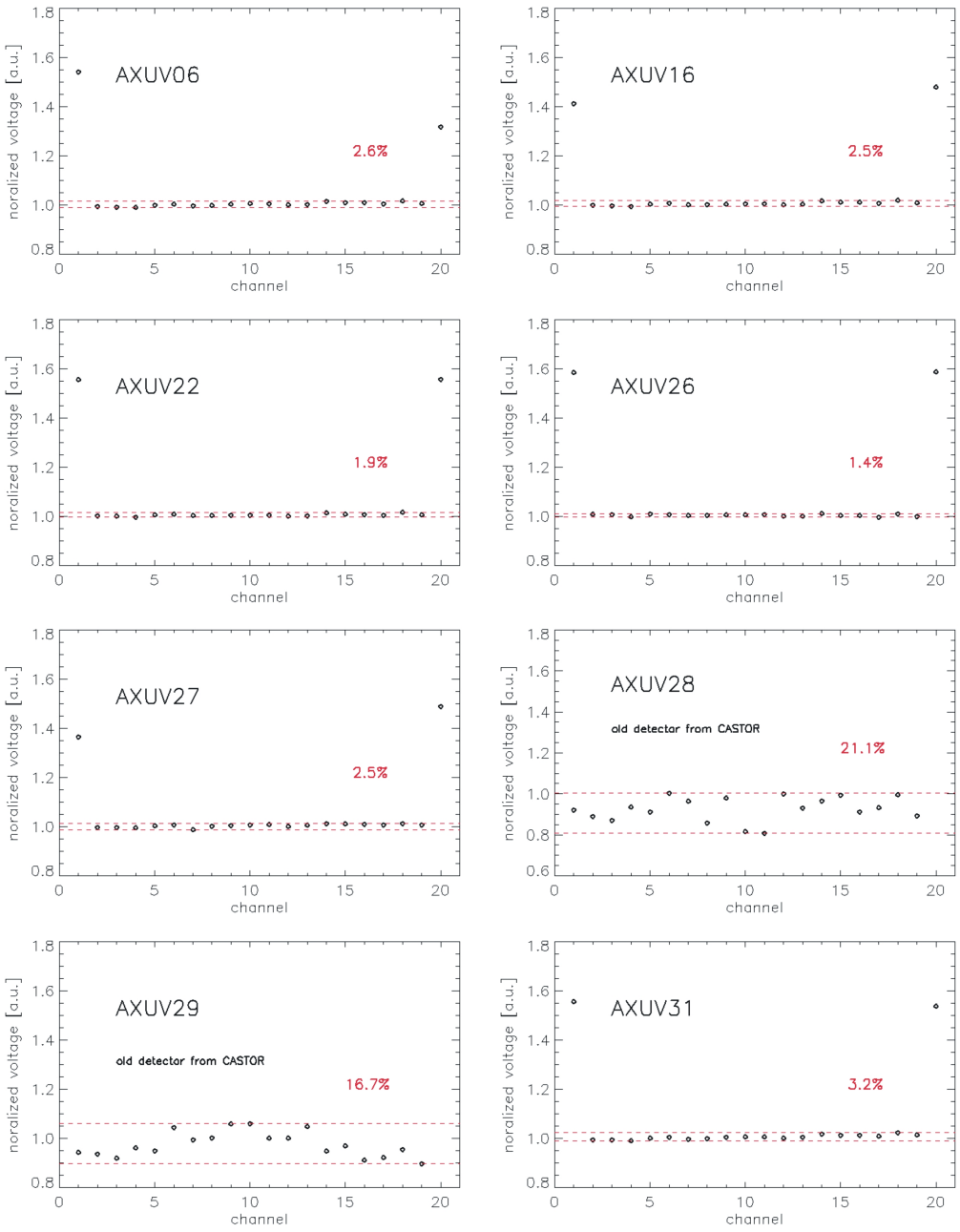

Figure 4.26: *Relative calibration of AXUV detectors, red dashed lines indicates the maximal dispersion of values*

Channel #	**Corr. factor**	**Channel #**	**Corr. factor**	**Channel #**	**Corr. factor**	**Channel #**	**Corr. factor**
1	0.65	6	1.00	11	1.00	16	0.99
2	1.01	7	1.00	12	1.00	17	0.99
3	1.01	8	1.00	13	1.00	18	0.98
4	1.01	9	1.00	14	0.99	19	0.99
5	1.00	10	0.99	15	0.99	20	0.76

Table 4.8: *Results of relative calibration for AXUV 06 detector array channels - correction factors normalized to channel #12*

Channel #	**Corr. factor**	**Channel #**	**Corr. factor**	**Channel #**	**Corr. factor**	**Channel #**	**Corr. factor**
1	0.71	6	0.99	11	1.00	16	0.99
2	1.00	7	1.00	12	1.00	17	0.99
3	1.00	8	1.00	13	1.00	18	0.98
4	1.01	9	1.00	14	0.98	19	0.99
5	1.00	10	1.00	15	0.99	20	0.68

Table 4.9: *Results of relative calibration for AXUV 16 detector array channels - correction factors normalized to channel #12*

Channel #	**Corr. factor**	**Channel #**	**Corr. factor**	**Channel #**	**Corr. factor**	**Channel #**	**Corr. factor**
1	0.64	6	0.99	11	1.00	16	0.99
2	1.00	7	1.00	12	1.00	17	1.00
3	1.00	8	1.00	13	1.00	18	0.98
4	1.00	9	1.00	14	0.99	19	0.99
5	1.00	10	1.00	15	0.99	20	0.64

Table 4.10: *Results of relative calibration for AXUV 22 detector array channels - correction factors normalized to channel #12*

Channel #	**Corr. factor**	**Channel #**	**Corr. factor**	**Channel #**	**Corr. factor**	**Channel #**	**Corr. factor**
1	0.63	6	0.99	11	0.99	16	1.00
2	0.99	7	1.00	12	1.00	17	1.00
3	0.99	8	1.00	13	1.00	18	0.99
4	1.00	9	1.00	14	0.99	19	1.00
5	0.99	10	0.99	15	1.00	20	0.63

Table 4.11: *Results of relative calibration for AXUV 26 detector array channels - correction factors normalized to channel #12*

Channel #	**Corr. factor**	**Channel #**	**Corr. factor**	**Channel #**	**Corr. factor**	**Channel #**	**Corr. factor**
1	0.73	6	0.99	11	0.99	16	0.99
2	1.00	7	1.01	12	1.00	17	0.99
3	1.00	8	1.00	13	0.99	18	0.99
4	1.01	9	1.00	14	0.99	19	0.99
5	1.00	10	0.99	15	0.99	20	0.67

Table 4.12: *Results of relative calibration for AXUV 27 detector array channels - correction factors normalized to channel #12*

Channel #	**Corr. factor**	**Channel #**	**Corr. factor**	**Channel #**	**Corr. factor**	**Channel #**	**Corr. factor**
1	1.09	6	1.00	11	1.24	16	1.10
2	1.12	7	1.04	12	1.00	17	1.07
3	1.15	8	1.17	13	1.07	18	1.00
4	1.07	9	1.02	14	1.04	19	1.12
5	1.10	10	1.23	15	1.01	20	err

Table 4.13: *Results of relative calibration for AXUV 28 (old CASTOR detector) detector array channels - correction factors normalized to channel #12*

Channel #	**Corr. factor**	**Channel #**	**Corr. factor**	**Channel #**	**Corr. factor**	**Channel #**	**Corr. factor**
1	1.06	6	0.96	11	1.00	16	1.10
2	1.07	7	1.01	12	1.00	17	1.08
3	1.09	8	1.00	13	0.95	18	1.05
4	1.04	9	0.94	14	1.05	19	1.11
5	1.05	10	0.94	15	1.03	20	err

Table 4.14: *Results of relative calibration for AXUV 29 (old CASTOR detector) detector array channels - correction factors normalized to channel #12*

Channel #	**Corr. factor**	**Channel #**	**Corr. factor**	**Channel #**	**Corr. factor**	**Channel #**	**Corr. factor**
1	0.64	6	1.00	11	0.99	16	0.99
2	1.01	7	1.00	12	1.00	17	0.99
3	1.01	8	1.00	13	1.00	18	0.98
4	1.01	9	1.00	14	1.00	19	0.99
5	1.00	10	0.99	15	0.99	20	0.65

Table 4.15: *Results of relative calibration for AXUV 31 detector array channels - correction factors normalized to channel #12*

Chapter 5

Reconstruction methods

The data collected by multichannel photodiodes mostly origin from volume, opticaly thin, isotropic and inhomogeneous source. Measurements using these diagnostics don't indicate the local radiated power. They provide signal integrated over the solid angle of their field of view. The principal aim of recontsruction methods is to determine the local properties of plasma radiation in every point of the poloidal cut from these integral measurements.

5.1 Abel inversion

If one assumes the toroidal symmetry of tokamak plasmas and subsequently focuses only on a poloidal cross-section (2D), for measured data $I_{view}(y)$ and distribution of radiation in space $I(x, y)$ we can write integral equation:

$$I_{view}(y) = \int_{-\sqrt{a^2-y^2}}^{\sqrt{a^2-y^2}} I\,(x, y)\,dx \tag{5.1}$$

The inverse solution of this equation is the distribution of radiation in space. In general this equation has no analytical solution. Fortunately, there are methods how to reach the solution in some special cases. Abel inversion is one of these methods [25], [26], which processes along chord integrated data from one direction and considers the radial symmetry of radiation.

Taking into account presumption of radial symmetry we can rewrite equation 5.1

using substitution $x^2 + y^2 = r^2$, where $dx = \frac{r}{\sqrt{r^2-y^2}}dr$. We get:

$$I_{view}(y) = 2\int_0^{\sqrt{a^2-y^2}} I(x^2+y^2)dx = 2\int_{|y|}^{a} I(r)\frac{r}{\sqrt{r^2-y^2}}dr \tag{5.2}$$

In case of "fan" ordered chords the rotational transformation is necessary:

$$I_{view}(x,\alpha) = I_{view}(x.sin\alpha) \tag{5.3}$$

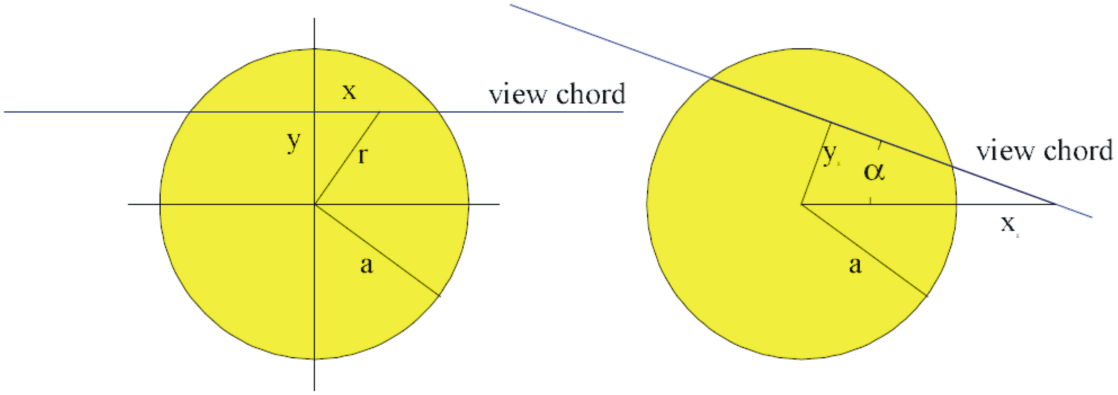

Figure 5.1: *Measurement of planar source radiation with parallel chords (left) and fan ordered chords (right)*

Equations 5.1 and 5.2 represent the direct Abel transformation. In multichanel spectroscopy we face the inverse problem, i.e. solve the inverse Abel transformation.

The inverse Abel transformation can be solved analyticaly or numericaly. Because of complexity of this problem, the numerical methods are prefered, e.g. [27]. The precise form of inversion is:

$$I(r) = -\frac{1}{\pi}\int_r^R \frac{dI_{view}}{dy}\frac{dy}{\sqrt{y^2-r^2}} \tag{5.4}$$

This reconstruction method fails for not fully symmetric radiation profiles. In these cases, it is possible to modify standard Abel transformation. The so called asymmetrical Abel inversion consider asymmetrical pertubation in direction perpendicular to observation chord [28], [29].

Considering asymmetry in vertical direction (direction of axis y) we can write:

$$I_{view}(y) = \int_{-\sqrt{a^2-y^2}}^{\sqrt{a^2-y^2}} I\left(r = \sqrt{x^2+y^2}, y\right) dx \tag{5.5}$$

$$I\left(r = \sqrt{x^2+y^2}, y\right) dx = g(y) I_s\left(r = \sqrt{x^2+y^2}\right) \tag{5.6}$$

where $-a \leq y \leq a$ and $0 \leq r \leq a$. Than

$$I_{view} = g(y) \int_{-\sqrt{a^2-y^2}}^{\sqrt{a^2-y^2}} I_s\left(r = \sqrt{x^2+y^2}\right) dx \tag{5.7}$$

$$I_{view} = 2g(y) \int_{0}^{\sqrt{a^2-y^2}} I_s(r) dx = 2g(y) \int_{|y|}^{a} I_s(r) \frac{r}{\sqrt{r^2-y^2}} dr \tag{5.8}$$

The function $g(y)$ is called weighting function, which prescribes the degree of asymmetry. For $g(y)$=1 we get axialy symmetric case mentioned above. The function I_s is even and we can get it as:

$$I_s = \frac{I(y) + I(-y)}{2} \tag{5.9}$$

$$g(y) = \frac{I(y)}{I_s(y)} \tag{5.10}$$

This adjustment simplifies the situation and it remains "only" to perform the inverse Abel transformation of even function:

$$I_s(y) = 2 \int_{|y|}^{a} I_s(r) \frac{r}{\sqrt{r^2-y^2}} dr \tag{5.11}$$

For these inversion we can use standard procedures descibed above.

In the real application of this method, the measured (simulated) data are smoothed with a curve in order to reduce the impact of random errors and fluctuations. Parameters of this curve are used for calculation of weighting function. The fitted curve is subsequently input for analytical or numerical symmetric Abel inversion.

For data fitting there are used polynomial functions

$$f(y) = A_0 + A_1 y + A_2 y^2 + A_3 y^3 + ... \tag{5.12}$$

Gauss distribution improved by polynomial

$$f(y) = A_0 e^{\frac{(y-A_1)^2}{A_2^2}} + A_3 + A_4 y + A_5 y^2 + ... \tag{5.13}$$

and triple Gauss distribution

$$f(y) = A_0 e^{\frac{(y-A_1)^2}{A_2^2}} + A_3 e^{\frac{(y-A_4)^2}{A_5^2}} + A_6 e^{\frac{(y-A_7)^2}{A_8^2}} \tag{5.14}$$

In order to improve the convergence of fitting function, zeros are added to boundaries of measured data. This convergence restricts the possibility of polynom oscilations near bourdariers and contributes to more physically relevant results of Abel inversion. The result of inversion is subsequently multiplied by weighting function and we get radiation reconstruction.

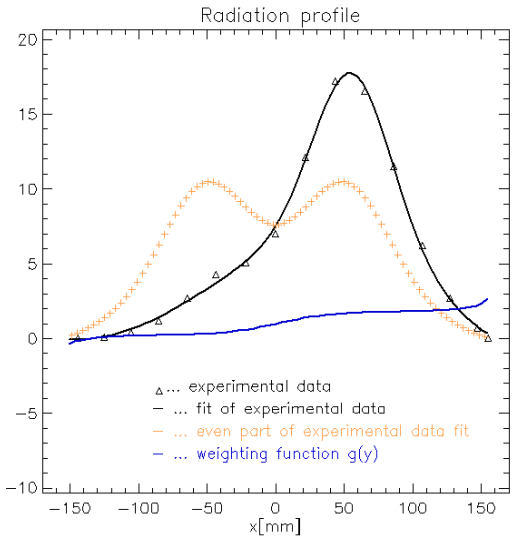

Figure 5.2: *Experimental data (triangles) its fit (black line) and even part (crosses), blue line indicates weighting function*

5.1.1 Simulations

The efficiency of Abel inversion was tested using test functions. It means, the spatial distribution of radiation was described using simple functions. Subsequently, these

functions were integrated along optical paths of real detectors to get the data input for Abel inversion. The reconstruction was performed and the result was compared with the original test function. For performance of these simulations, the procedure was written in programming environment IDL.

Because in the first phase of the COMPASS tokamak operation, the plasma will have circular cross-section, the test functions are limited by circle with 16cm diameter (supposed plasma diameter 16 - 23 cm).

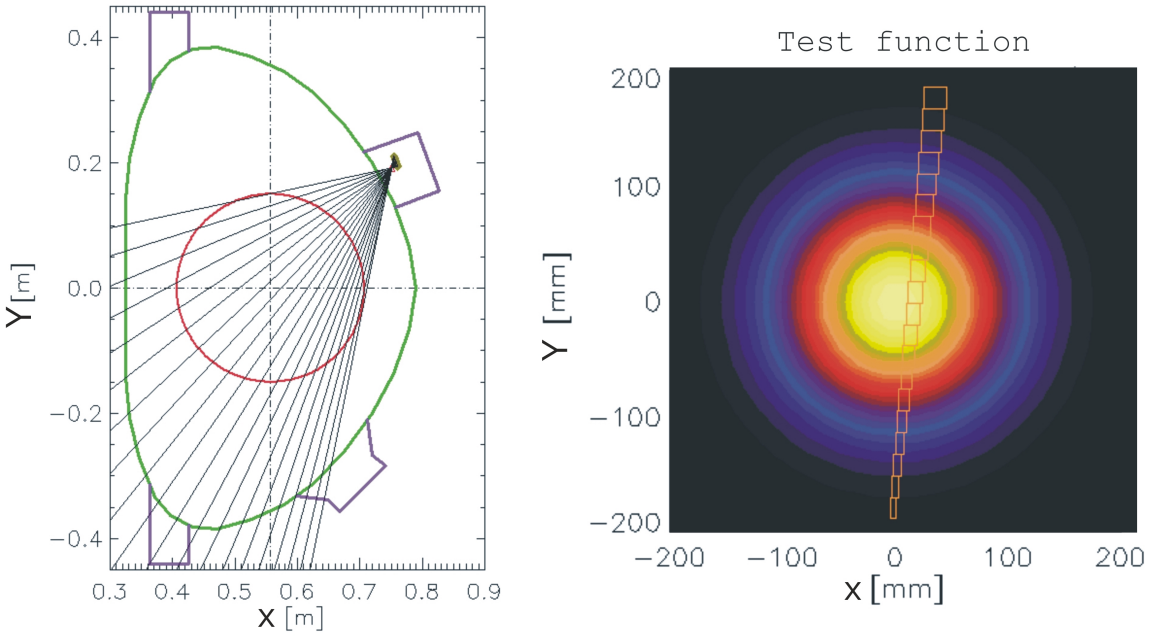

Figure 5.3: *Geometry of AXUV 1 detector with supposed plasma shape - red circle (left), detail of one chord integration, which is for visualization divided only to 20 intervals (right)*

The test functions are defined in cartesian coordinates. For example, in case of centrally symmetric plasma, it is obtained as:

$$f = ae^{b(x-m)^2+c(y-m)^2} \tag{5.15}$$

where a, b, c are coefficients determining shape and m, n are coordinates of function centre. The complicated shapes were defined as a sum of several such functions.

For simulations of Abel inversion reconstructions, AXUV 1 detector geometry was

used. In order to simplify the evalution, the whole calculation is carried out in normalized dimension units and the conversion back to milimeters is the last step of procedure.

At the beginning we need to sum the test function radiation along every chord. For this purpose, the chord is divided to intervals (typically 2000). Because we want to obtain radiation from surface, the lenght of interval has to be multiplied by the width of the field of view. Because of large plasma radius, we can't consider this width as constant and it is assumed as linearly increasing. The obtained rectangle is multiplied by value of test function in it's centre and resulting value is added to the sum of total radiation along chord.

By repeating of this procedure for all chords we obtain the data for all detectors. They represents the total radiation measured by one chord over the whole test function. These data are used as an input to reconstruction.

In general, there were prepared six approaches to Abel inversion. Analytical and numerical inversion were used, both using fits with polynomial, Gauss improved with polynomial or sum of three Gausses. By reconstructions of test functions, it appeared that the numerical inversion (especially using polynomial and improved Gauss fit) is reaching better results than analytical, which is strongly limited by a small number of used terms (analytic integration was done in a software environment of Maple). The addition of zero points at borders of data appeared as a usefull tool for restriction of oscilations in periphery regions.

In fig.5.4 there is shown an example of test function and its reconstruction using asymmetrical Abel inversion for the simpliest test function - central peak. For reconstruction the numerical method with improved Gauss fit was used.

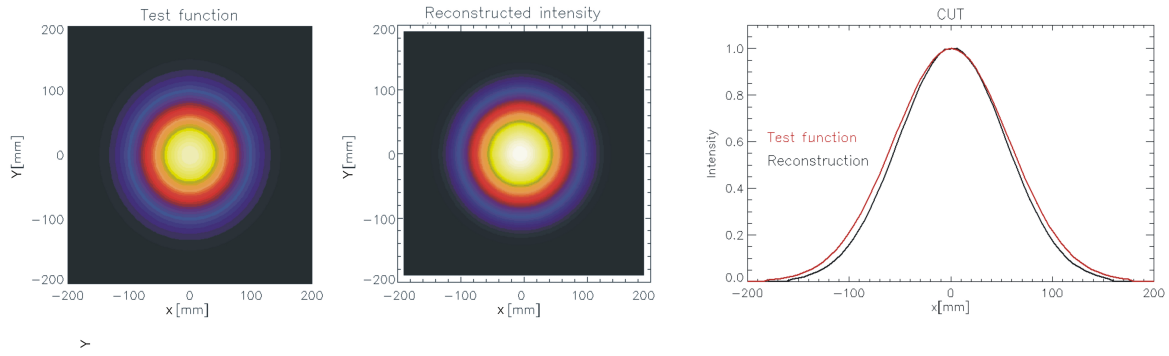

Figure 5.4: *Test function (left) and its reconstruction (middle) performed using asymmetrical Abel inversion, cut along axis x (right)*

For further reconstructions it is considered that the central channel of the detector

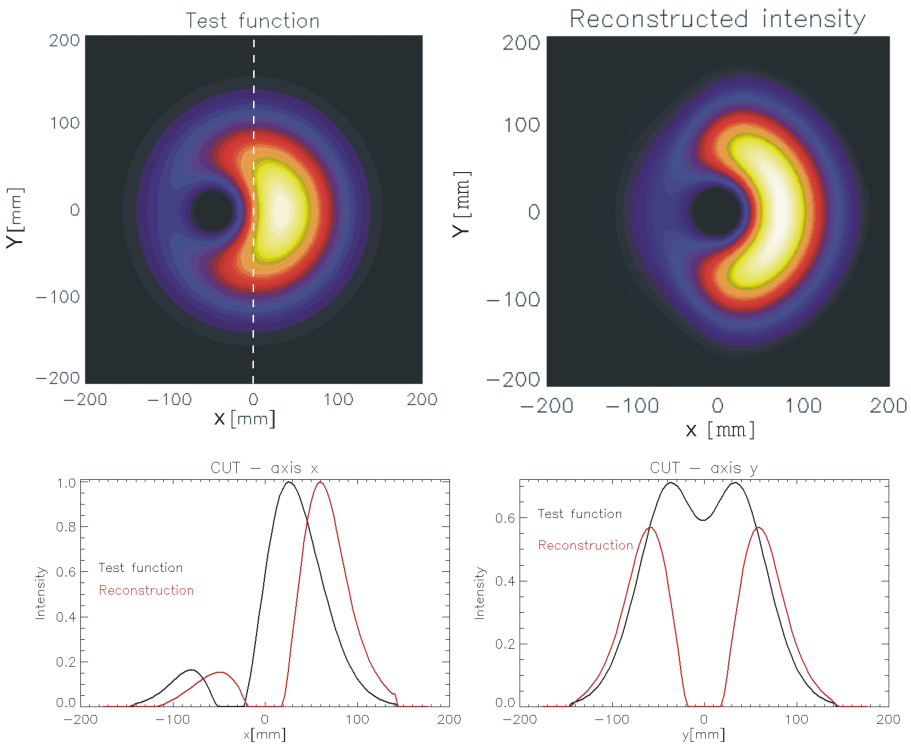

Figure 5.5: *Test function (up-left) and its reconstruction (up-right) performed using asymetrical abel inversion, the white dashed line indicates the central channel direction of view, cuts of functions along axis x (down-left) and along axis y (down-right)*

observes the plasma along the y axis (see fig. 5.5). That means, the plasma profile is rotated around it's centre. This assuption significantly simplifies the reconstruction procedure and do not influence a functionality test of the method.

The fig.5.5 shows reconstruction of test function, which has along the x axis perturbated radial symmetry, but in perpendicular direction (axis y and also view of central channel) it is symmetric. These conditions are exactly suitable for asymmetrical Abel inversion. For reconstruction the numerical method with improved Gauss fit was used again.

In the opposite case, when the presumption of radial symmetry in direction perpendicular to direction of chords is perturbated, the asymmetrical Abel inversion fails for both integration methods and their fits (see fig. 5.6).

Asymmetrical Abel inversion is very useful method for radiation profile reconstruc-

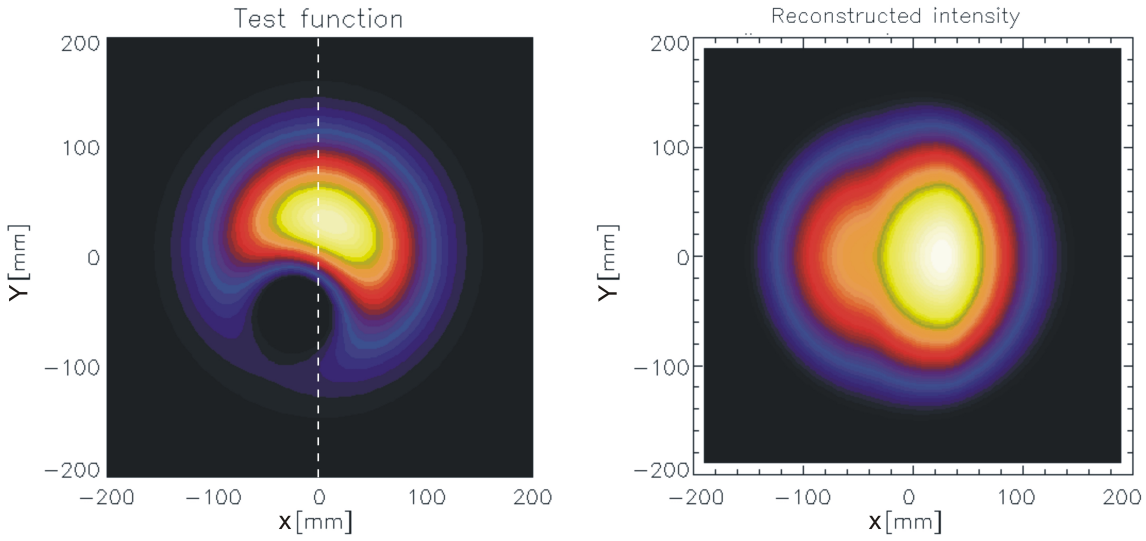

Figure 5.6: *Test function (left) and its reconstruction (right) performed using asymmetrical Abel inversion, the white dashed line indicates the central channel direction of view*

tions because of it's simplicity. However, for data with complex structure it isn't always succesful. Precise results are obtained only in case of highly symetric profiles, but actually a major part of real measurements will not satisfy this requirements. Nevertheless, this method is suficient for rough estimation of plasma radiation space distribution. For more accurate reconstructions, tomographic methods have to be used. One of them, which will be used on the COMPASS tokamak, is described in the next section.

5.2 Cormack method

Tomography is a computation method, which reconstructs from measurements in several diferent directions the radiation distribution of an object [30],[31],[32]. The general principle is following:

The distribution of radiation in space is described by function $g(r, \theta)$. As a projection of this function we get function $f(p, \phi)$. Then location of viewing chords can be parametrized by polar coordinates (see fig. 5.7). Intensity measured along one chord is then:

$$f(p, \phi) = \int_{L(p,\phi)} g(r, \theta) dL \tag{5.16}$$

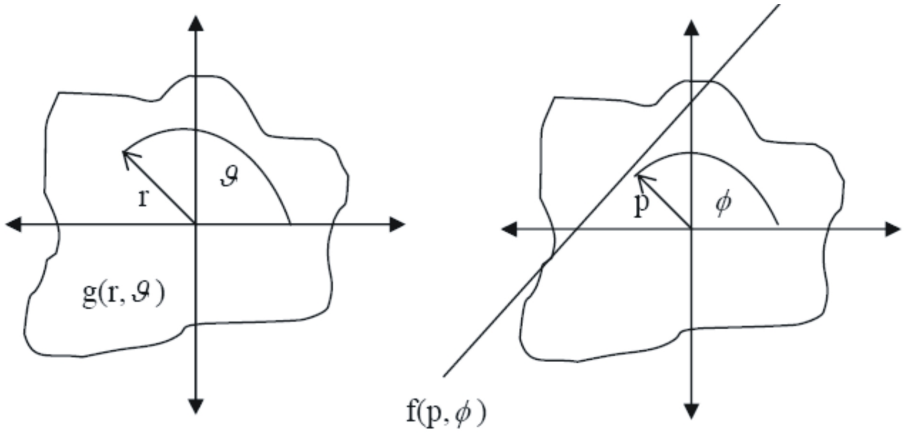

Figure 5.7: *Functions* $g(r,\theta)$ *and* $f(p,\phi)$

The function g is the wanted polynom, which describes the radiation disribution in space. For it's determination, we have to solve 5.16.

Widely used Cormack method is one possibility how to find the solution for relatively simple and smooth radiation profiles [33], [34]. Functions $g(r,\theta)$ and $f(p,\phi)$ can be expressed in harmonical components containing sinus and cosinus:

$$g(r,\theta) = \sum_{m=0}^{\infty} [g_m^c(r)cos(m\theta) + g_m^s(r)sin(m\theta)] \tag{5.17}$$

$$f(p,\phi) = \sum_{m=0}^{\infty} [f_m^c(p)cos(m\phi) + f_m^s(p)sin(m\phi)] \tag{5.18}$$

In this expansion, it is sumed over infinite amount of components. In reality there is limited amounth of detectors, thus the number of components of measured projection $f(p,\phi)$ is also limited. It means sums have to be finite.

By using an expansion to Chebyshev polynomials in 5.18 we obtain:

$$f(p,\phi) = \sum_{m=0}^{M}\sum_{l=0}^{L} [a_{ml}^c(p)cos(m\phi) + a_{ml}^s(p)sin(m\phi)] \frac{2}{m+2l+1} U_{m,l,p} \tag{5.19}$$

where $U_{m,l,p}$ is Chebyshev polynomial defined as:

$$U_{m,l,p} = sin\left[(m+2l+1)arccos(p)\right] \tag{5.20}$$

where M is maximal number of independent sights on area with radius p, m is called „poloidal mode number“ [2], and L is number of chords on one detector.

Next the measured data are fitted with 5.20 using method of least squares. With these procedure we obtain coeficients $a_{ml}^{c,s}$. Coeficients $g_m^{c,s}(r)$ from expansion of $g(r,\theta)$ 5.17 is possible to calculate as:

$$g_m^{c,s}(r) = \sum_{l=0}^{L} a_{ml}^{c,s} R_{ml}(r) \tag{5.21}$$

The functions $R_{ml}(r)$ are Zernike polynomials defined as:

$$R_{ml}(r) = \sum_{s=0}^{l} r^{m+2l-2s} \frac{(-1)^s (m+sl-s)!}{s!(m+l-s)!(l-s)!} \tag{5.22}$$

Finally, we insert values of $g_m^{c,s}(r)$ to expansion of $g(r,\theta)$ 5.17 and we obtain the wanted space distribution of radiation.

5.2.1 Simulations

The efficiency of Cormacks method was tested using the same test functions as in case of Abel inversion. Also the input data were obtained from the test function with the same procedure.

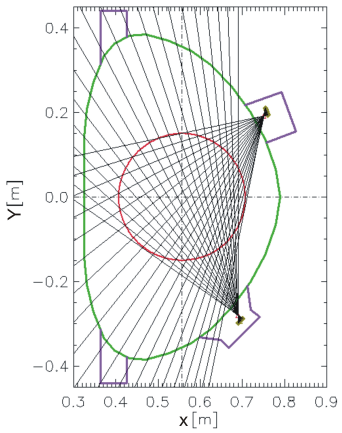

Figure 5.8: *Geometry of AXUV 1 (upper port) and AXUV 3 (lower port) detectors with supposed plasma shape (red circle)*

The Cormack method process data from more than one detector (direction). For simulations we confine to two detectors. AXUV 1 detector geometry was used for the

first detector. For the second one we assumed geometry of proposed detector in lower angular port marked as AXUV 3 (see fig. 5.8). The views of central channels of these detectors are perpendicular. In reconstructions we consider that central channel of AXUV 1 observes plasma along the x axis and central channel of AXUV 3 along the y axis.

The whole reconstruction is carried out in normalized dimension units and the conversion back to milimeters is the last step of procedure.

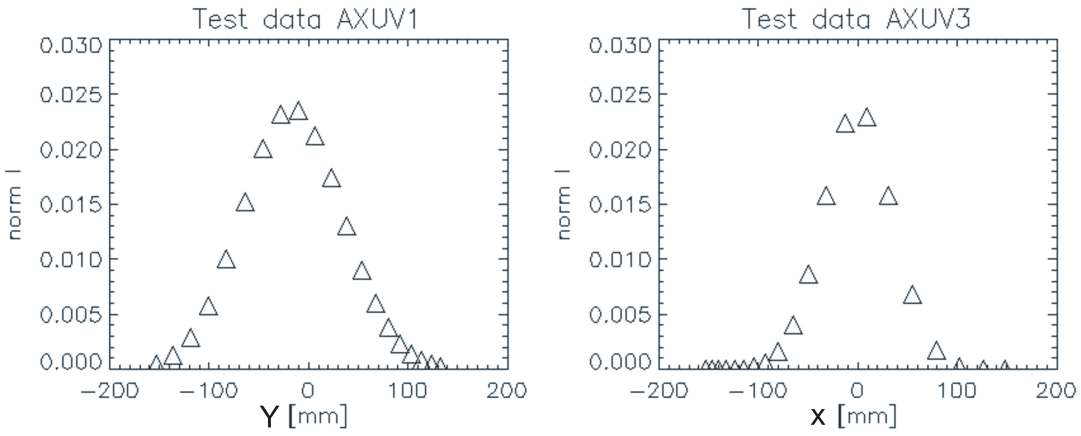

Figure 5.9: *Example of data obtained from test function for AXUV1 and AXUV3*

The example of data obtained from the test function for both detectors are plotted in fig. 5.9. These values are the input data to the thomographic reconstruction.

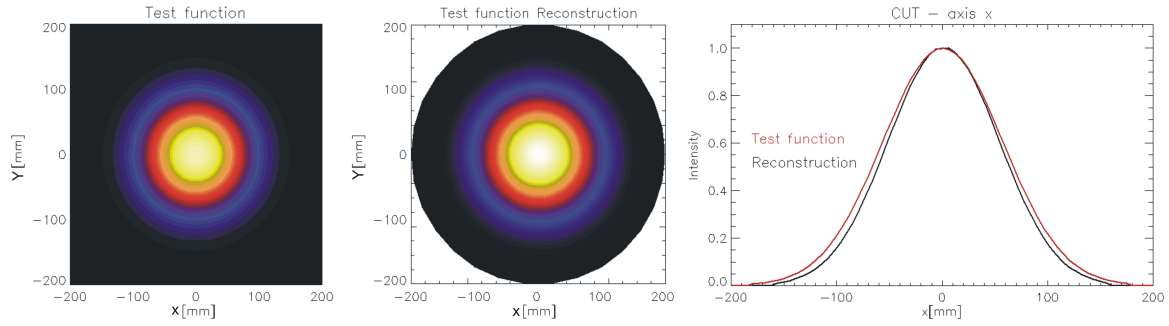

Figure 5.10: *Test function (left) and its tomographic reconstruction (middle) performed using Cormack method, cut of functions along axis x(left)*

The results of tomographic reconstructions are show in figs. 5.10,5.11 and 5.12. As supposed the Cormack method provides more precise reconstructions than asymmetrical Abel inversion. Even the more complex shapes of radiation profile were reconstructed with high accuracy. The detailed discussion of Cormack method effectivneess for wide spectrum of test profiles and also examples of real data reconstructions can be found in [35].

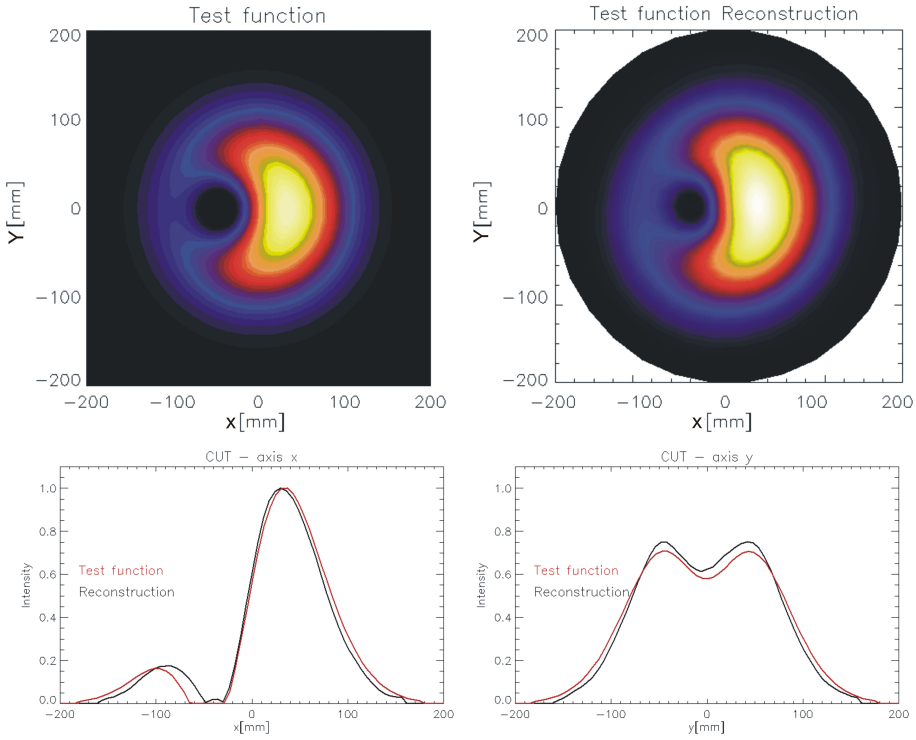

Figure 5.11: *Test function (up-left) and its tomographic reconstruction (up-right) performed using Cormack method, cuts of functions along axis x(down-left) and along axis y (down-right)*

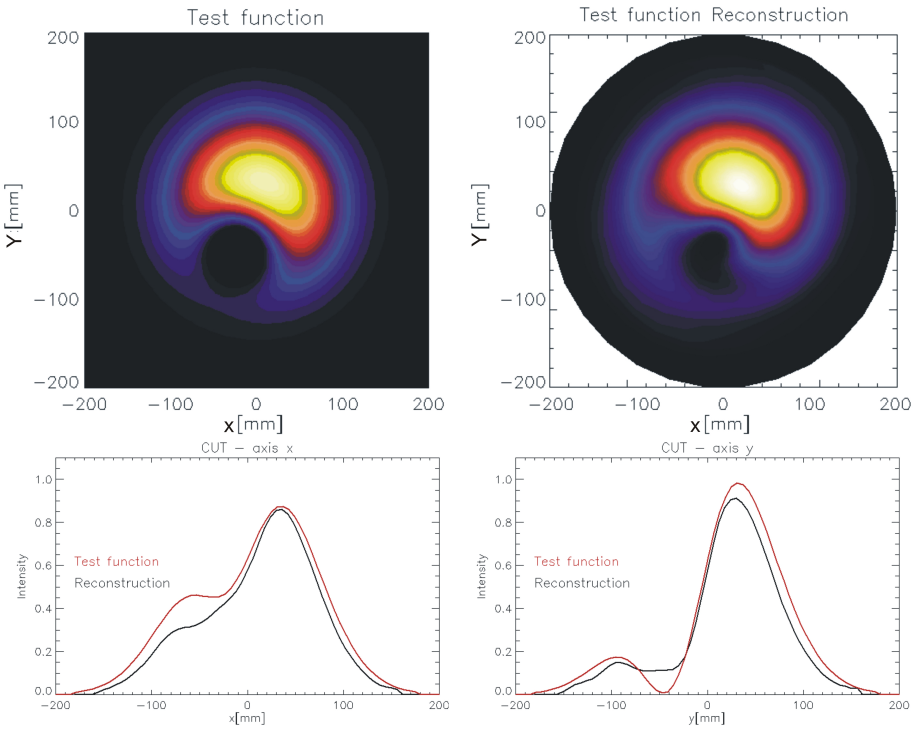

Figure 5.12: *Test function (up-left) and its tomographic reconstruction (up-right) performed using Cormack method, cuts of functions along axis x(down-left) and along axis y (down-right)*

Chapter 6

Conclusion

There are various radiation processes in tokamak plasma, presenting a wide range of possible energy losses. The semiconductor detectors, intended for the measurement of radiated power, provides the suitable tool for monitoring of plasma radiation with high temporal resolution.

In the frame of this thesis, the first phase of the development of new bolometric and SXR diagnostic systems for the COMPASS tokamak, based on these detectors, was solved.

AXUV-20EL photodiode arrays (20 channels), with spectral range from ultraviolet up to soft X-rays, were chosen as bolometers and LD35 (JET) WINDOWLESS photodiode arrays (35 channels) were chosen for measurement of radiation in soft X-ray region. Both these detectors are characterized mainly by high temporal resolution and small size. The used principle of camera obscura provides the possibility of spatialy resolved measurements.

The geometrical setup of detectors inside port and positioning of pinholes were calculated as a compromise between plasma covering and spatial resolution. Considering these parameters, the special port plug assembled from two pieces was developed. The first component holds two AXUV's, one SXR detector and also their replaceable pinholes. There is also space for objective for visible light spectroscopy (VIS). Simultaneously, it provides the shutter to prevent detectors and optics (VIS) from an impurity layers deposition during cleaning glow discharge, an internal cooling to prevent detectors from overheating during vacuum vessel baking and thermocouples for temperature monitoring. The second part is the NW100 flange with two electric feedtroughs (each 41 pins), which handles signals from detectors, and with holes for VIS and shutter.

Two prototypes of amplifier boxes with cable input optimized as counterpart for the air side of vacuum feedthrough were constructed. These boxes always take care for all

signals from the feedthrough. Each amplifier has the two-stage structure. In the first stage, the measured current is transformed into voltage and pre-amplified, in the second stage this voltage is amplified. The final rate between input current and output voltage was choosen as $6.3x10^5$ for SXR amplifiers and $5.2x10^5$ for AXUV amplifiers (but it can be changed according to future experimental needs). The cables, using high-frequency telecommunication standards, for signal hadling from amplifiers up to data acquisition system, were also prepared.

In order to measure characteristics of amplifiers and also to test functionality of detectors, prototypes of amplifiers applicable to simple laboratory measurements were constructed. Using these measurements, parameters of final amplifiers were optimized and subsequently the typical responses of detector-amplifier system were measured. From these tests the time resolution of detector-amplifier system appears to be better than 5μs.

To control fabrication-related spread of responsitivity and differences in amplification, a relative calibration to weight the detectors response among each other was realized. Initially a relative calibration of the amplifier channels was done. Subsequently, the relative calibration of detectors was done using standard halogen lamp as the source. These tests indicates that differencies of sensitivity between particular diodes on detector array for SXR detectors ranges from 5.9% up to 11.7% and from 1.4% up to 3.2% for AXUV's. The significant increase of dispersion (20%) was measured for old AXUV's, which were used on CASTOR tokamak.

The data collected by multichannel photodiodes don't indicate the local radiated power. They provide only signal integrated over the solid angle of their field of view. In order to get the local distribution of plasma radiation, two reconstruction methods were tested - asymmetrical Abel inversion and Cormack tomographic method. Abel inversion is intended for processing data from one detector array and requires at least partial radial symmetry of plasma profile to be assumed. The Cormack method compiles measurements from more detectors (in simulations two perpendicular detectors were considered). The tests on test functions indicate that Cormack method is able to reconstruct even more complex profiles with a high accuracy.

In future, it is planned to install next detectors in diagnostic ports at the same poloidal cross-section as the present detectors. This assembly will provide the full coverage of D-shaped plasma profile and it will improve the spatial resolution and thus allow the tomographic reconstruction.

Bibliography

[1] Chen F.F. Úvod do fyziky plazmatu. *Academia, Praha*, 1983.

[2] Wesson J. Tokamaks. *Caledon Press, Oxford*, 2004.

[3] Pánek R. et al. Reinstallation of the COMPASS-D Tokamak in IPP ASCR. *Czechoslovak Journal of Physics, Suppl. B*, 56, 2006.

[4] A. Mück. Study of the Sawtooth Instability and its Control in the ASDEX Upgrade Tokamak. *PhD thesis, IPP Garching*, 2004.

[5] Zohm H. ASDEX Upgrade Letter No. 7/March 2005. *Max-Planck-Institut für Plasmaphysik, Garching*, 2005.

[6] Wade M.R. Impurity enrichment and radiative enhancement using induced SOL flow in DIII-D. *Journal of Nuclear Materials*, 266-269:44–50, 1999.

[7] Seaton M.J. The Theory of Excitation and Ionization by Electron Impact. *Atomic and Molecular Processes, D. R. Bates Ed., New York*, 1982.

[8] Rice J.E. et al. X-Ray and VUV Observations of Mo^{23+}-Mo^{33+} Brightness Profiles from Alcator C-Mod Plasmas. *J. Phys. B*, 29:2191, 1996.

[9] Latter R. Karzas W.J. Electron Radiative Transitions in a Coulomb Field. *Astrophys. J. Suppl. Ser.*, 6:167, 1961.

[10] Nakel W. Haug E. The Elementary Process of Bremsstrahlung. *World Scientific*, 2004.

[11] Marr G.V. Plasma Spectroscopy. *Elsevier Publishing Company, England*, 1968.

[12] Lightman A.P. Rybicki G. Radiative Processes in Astrophysics. *Wiley-Interscience, New York*, 1979.

[13] Mattioli M. De Michelis C. Soft X-ray Spectroscopic Diagnostics of Laboratory Plasmas. *Nuclear Fusion*, 21:6, 1981.

[14] Weler A. et al. Modeling of Soft X-Ray Emission from JET Plasmas. *JET-IR*, 1987.

[15] Ingesson L.C. et al. Chapter 7, Tomograhy diagnostics. *Fusion Science and Technology*, 53, 2008.

[16] International Radiation Detectors. 2527 West 237th Street Unit C, Torrance, CA 90505-5243. 2000.

[17] National Institute of Standards and Technology. Absolute spectral responsitivity of International Radiation Detectors silicon photodiode model AXUV-100G. *NIST test #39080S*, 2000.

[18] Nachtrieb R. T. et al. Electron Cyclotron Discharge Cleaning Experiments on Alcator C-Mod. *Technical Report PSFC/JA-98-17, MIT*, 1998.

[19] Ingesson L.C. et al. Soft X-ray Tomography during ELMs and Impurity Injection in JET. *JET–P(98)02*, 1998.

[20] Igochine V. et al. Overview of SXR Diagnostic Upgrades for the 2007 Experimental Campaign. *AUG Core Physics Forum*, 2007.

[21] Centronic Limited. King Henry's Drive, Croydon, Surrey CR9 0BG. 2003.

[22] Ingesson L.C. et al. Optimization of apertures and collimators for multichannel plasma diagnostics. *Rev.Sci.Instrum.*, 73, 2001.

[23] Naydenkova D.I. et al. Design of New Optical System for Visible Plasma Radiation Measurements at COMPASS Tokamak. *WDS 2008, Prague, Czech Republic*, 2008.

[24] Šesták D. et al. Design and engineering of optical diagnostics for COMPASS. *25th Symposium on Fusion Technology, Rostock, Germany*, 2008.

[25] Schlatter Ch. Radiation loss studies on T-10 tokamak using AXUV-detectors. *diploma thesis, EP Lausane*, 2003.

[26] Weinzettl V. Prostorové a časové chování lehkých nečistot ve vysokoteplotním plazmatu tokamaku CASTOR. *PhD thesis, KFE FJFI CVUT, Prague*, 2005.

[27] Weinzettl V. et al. Snake-like structures after pelet injection in the T-10 tokamak. *Book of abstracts, Frascati, Italy : Associazione EURATOM-ENEA sulla Fusione,P4.080*, 2006.

[28] Yasumoto Y. et al. A New Numerical method for Asymmetrical Abel Inversion. *IEEE Transactions on Plasma Science, vol. PS-9,no.1*, 1981.

[29] Kalal M. Nugent K.A. Abel inversion using fast Fourier transforms. *Appl. Opt. 27*, 1988.

[30] Smeulders P. Fast plasma tomography with second order accuracy and compensation for spatial resolution. *IPP 2/252*, 1981.

[31] Furno I. The tomographic problem in plasma physics. *EPFL, Lausane*, 1995.

[32] Carvalho P.J. et al. Fast tomographic methods for the tokamak ISTTOK. *Plasma and Fusion Science: 17th IAEA Technical Meeting on Research Using Small Fusion Devices. AIP Conference Proceedings, Volume 996, pp. 199-206*, 2008.

[33] Cormack A.M. *Journal of Applied Physics 35, 2908*, 1964.

[34] Zahrt J.D. et al. Tomography: the Cormack algorithm revisited. *Nuclear Science Symposium and Medical Imaging Conference, 2048 vol.3*, 1991.

[35] Dufková E. Bolometrická měření celkového vyzářeného výkonu vysokoteplotního plazmatu tokamaku CASTOR. *BcS thesis, KFE FJFI CVUT, Prague*, 2009.